Bubble bursts in mud:
White Island observations and insights from laboratory experiments

A thesis submitted in partial fulfilment of the requirements for the Degree of

Master of Science in Geology

at the University of Canterbury

by

Matt Edwards

November 2015

Frontispiece

Small ~1 m mud pool bubbling on the Central subcrater floor with steam rising from the crater lake in the background. White Island, October 2015.

Acknowledgements

This thesis was made possible with the help and support of many people. I extend huge thanks to..

- Ben Kennedy for providing the opportunities with this project (and past ones) which have set me up for the future.
- Arthur Jolly for also supervising and introducing me to new fields of geology.
- Bettina Scheu for inviting me to LMU and the discussions around this topic.
- Philippe Jousset for similar discussions.
- Jacopo Taddeucci for his guidance and assistance during my time at INGV and after (and the invite to Stromboli!)
- the other INGV staff who helped along the way.
- Pierre-Yves Tournigand for hosting me in Rome.
- Diana Schmid for taking the time in showing me your work at LMU.
- the UC staff.
- Kate Dobson for offering a room in Munich on such short notice.
- Brad Scott and his wife Judy for hosting me at their home in the early stages of this work.
- PeeJay tours and Frontier Helicopters for access to their video recordings from White Island.
- Hayden Inman who provided his personal recordings.
- Mason Trust and GNS for their financial support.
- My family for the support throughout the past year.

Table of Contents

List of Figures

List of Tables

Thesis Abstract

Phreatic eruptions are common in the recorded history of White Island, New Zealand. Although the larger eruptions have been described in literature, little attention has yet been given to the smaller, more frequent phreatic activity. In addition, the style in which steam bubbles are released during phreatic eruptions at the surface can be highly variable and is poorly understood.

Throughout 2013, multiple episodes of phreatic bubble bursts in a mud-sulphur pool occurred at White Island. The first of these episodes, lasting from January 15 to February 7, was well preserved in the video record by GNS staff, tourists and tour operators. Analysis of these videos showed that the mud surface expressions of rising bubbles varied over this period as the apparent high water fraction of the mud pool was first depleted and then regained. Here, these expressions are classified into four regimes, which progressed from 1) low ~8 m, highly fluidal structures to 2) brittle 'starbursting' of hemispheres and heaves of ~40 m height to 3) rapid gas jets followed by high heaves up to ~102 m and finally 4) dry mud venting up to ~67 m height with the complete pool desiccation. Regression back through these regimes from January 30 coincided with the pool returning to the initial fluidal state and a similar depth.

Experimental modelling of bubble bursts in mud was conducted in order to identify the influence of viscosity and bubble shape, length and depth on the White Island regimes. An analogue to the White Island mud was created by mixing of kaolinite powder and water to controlled ratios. Bursts were performed at depths of 0.5, 5 and 10 cm in 9 different mud ratios corresponding to an increasing viscosity. Results of these experiments show that viscosity has a negative influence on heave heights but controls the transition from fluidal to brittle structures. Importantly, both a shallowing of bubble depth and an increase to bubble length are shown to increase the height of heaves.

Relating experimental results to White Island observations provides insight to bubble processes not observable in the video record. The higher heaves observed in conjunction with viscosity increase imply that bubble morphology or depth must be varying throughout the episode. Here, increases in bubble length towards long, conduit-controlled slug-shaped bubbles is shown to be a possible mechanism for the increasing ejection heights. Decrease of the mud pool level by desiccation, results in shallower bubble depths, and is also considered to be an influence to the observed increased explosivity. The more brittle behaviour of bubble bursts and mud heaves is shown to be related to the increasing viscosity of the mud pool. These results ultimately fill an absence in knowledge of phreatic processes occurring at White Island.

The evolution of the White Island eruption to more explosive regimes ejected ballistics to increasing distances. Similar bubble processes are associated with other volcanic and geothermal systems such as lava lakes and geysers. Evolution of eruptions at these systems could therefore result in similar ballistic hazards. Understanding the processes responsible for the White Island evolution may provide insight and improve hazard assessments at White Island and other systems around the globe.

Chapter 1. Introduction

1.1 Overview

Phreatic eruptions are common forms of volcanism in volcano-hydrothermal systems around the world (Barberi et al., 1992; Letham-Brake, 2013; Fitzgerald et al., 2014; Kato et al., 2015). Although eruption styles are highly variable, steam bubble release following the heating of water is the driving mechanism in all phreatic activity (Buttenelli et al., 2011). This steam release can be violent with the ability to eject overlying blocks on a km scale (Fitzgerald et al., 2014) or more passive, as bubble bursts in overlying crater lakes (Morrissey et al., 2010). All of these eruptions differ from other volcanism by the absence of any direct magmatic component, although deeper magma bodies are an indirect source of heating (Germanovich & Lowell, 1995; Browne & Lawless, 2001). Hazard and risk assessment for phreatic eruptions can be difficult due to the often limited or absent precursory signals (Barberi et al., 1992) and the ability of eruption styles to evolve over time.

White Island volcano, New Zealand, hosts a long-established, shallow volcano-hydrothermal system (Giggenbach & Glasby, 1977; Nishi et al., 1996). This typically expresses at the surface as fumaroles, a crater lake and streams, mud pools and hot springs. Multiple phreatic episodes in the historic record however illustrate the potential for much more explosive events (Letham-Brake; 2013). While some of these have been described previously (e.g. 1976-1982 events: Houghton & Nairn, 1989) little attention has yet been given to the smaller, more frequent phreatic activity.

This thesis is a step towards increasing the knowledge of the range of phreatic eruptions at White Island. Information gained provides insight to processes of bubble ascent and eruption evolution. Furthermore, results of this study may be applied to other volcanoes and geothermal systems to improve hazard and risk assessment.

1.2 Outline of Thesis Structure

This thesis is structured in the following way:

Chapter 1: An overview of the study and introduction of aims and research questions. This chapter includes definitions of key terminology used within this thesis. This chapter has been kept concise to avoid repetition with introduction sections for individual chapters.

Chapter 2: This chapter covers the January and February phreatic eruption episode on White Island in 2013 and takes the form of a paper prepared for publication. Co-authors (Ben Kennedy, Arthur Jolly, Bettina Scheu and Philippe Jousset) provided comment on an early version of this chapter and the expertise in processing the acoustic and seismic data. Following thesis submission, co-authors will provide greater input to make this chapter suitable for publication in the Journal of Volcanology and Geothermal Research.

Chapter 3: This chapter covers the experimental phase of the study involving the systematic bubble burst experiments in mud. The evolution of bubble morphology during ascent is also investigated to identify how surface expressions are formed.

Chapter 4: This chapter forms a discussion linking regimes identified in mud experiments with regimes identified at White Island. Inferences are made from experimental results on the evolution of bubble morphology at White Island.

1.3 Project Aims and Research Questions

This research focuses on the surface expressions of bubble ascent and burst in mud. A two step approach is taken in this study, including 1) a detailed analysis of the January/February phreatic episode at White Island in 2013, and 2) experimental modelling and analysis of bubble bursts using balloons in a mud-filled tank.

From these steps, the research questions that this study investigates are:

1. How does the eruptive style evolve during the White Island episode?
2. What implications does this evolution have in terms of hazards at this and other volcanoes?
3. How do the variables of mud viscosity, and bubble shape, length and depth control surface expressions?
4. Which of these variables are responsible for producing the evolving eruptive style at White Island?

1.4 Terminology

Several terms used within this thesis are either absent or display a range of definitions in the current literature. As such, these terms in this study are defined below.

Hemisphere: A dome-shaped upwelling of a mud or water surface by ascent of a gas/steam bubble.

Heave: The secondary upheaval of material following some form of primary gas release. The mechanism responsible for this feature is discussed in Chapter 3.

Slug: An elongate bubble which occupies the entire width of a conduit. In experiments where width is constrained initially by the balloon walls, the term slug refers to the overall elongate shape.

Phreatic eruption: An eruption caused by the heating of water to steam by proximity of a magma body.

Chapter 2. Evolution of phreatic eruption regimes through a mud pool, White Island, NZ.

2.1 Abstract

White Island volcano, New Zealand was host to multiple phreatic eruptive episodes within a mud-sulphur pool in 2013. Although phreatic activity is common at White Island, past events have largely gone undescribed in favour of the larger phreatomagmatic and magmatic eruptions. Here, we detail the first and longest phreatic episode of 2013, lasting from January 15 to February 7. Differences in bubble burst style across this episode lead to the classification of four distinct regimes. Each of these are associated with an increasing viscosity of the pool from an initial high-fluidity mud to a complete desiccation. Heaves, or secondary upheaval events following primary hemisphere formation or gas jets, increase in height from ~8 m during Regime 1 on January 15 to ~102 m during Regime 3 on January 28. Dry mud venting of Regime 4 develops on January 29 before a regression back to Regime 1 by February 7 as the pool re-establishes. Through observations of heaves and ejected clast morphologies we propose that the increasing explosivity of regimes is primarily due to increasing slug bubble lengths and mud pool viscosity. We attribute a lesser control to a shallowing of bubble depth as a result of desiccation and decreasing surface level of the mud pool. Occasionally visible yellowing of the steam/gas plume has led to suggestion that this sulphur component is indicative of a phreatomagmatic eruption. However, we argue in favour of a purely phreatic eruption and attribute visible sulphur to re-melting and mobilisation of existing elemental sulphur. The varying degree of explosivity throughout the episode implies a new consideration in assessing eruption hazards.

2.2 Introduction

Eruptions involving volcano-hydrothermal systems are common but show large variation in style and generation processes. At the lower end of the scale are hydrothermal eruptions related to transient pressure changes in the near-surface portion of underlying hydrothermal systems (Hedenquist & Henley, 1985) and do not involve direct magmatic heating (Germanovich & Lowell, 1995). Phreatomagmatic eruptions define the upper end of the scale as the result of the violent interaction of a magma source with groundwater (Valentine et al., 2014). The focus of this paper are the phreatic eruptions, which place in between these two extremes. Inconsistencies exist in the literature concerning use of the term phreatic in eruption classifications. This leads us to define phreatic eruptions as those where steam produced by heating of water in proximity to a magma source is the driving component. Any ejected material consists of country rock or overburden (including suspended particles in water bodies) with a characteristic absence of any juvenile material. White Island has displayed the complete range of these eruption styles in its recorded history (Letham-Brake, 2013; Mayer et al., 2015).

Phreatic eruptions alone have a diverse range of eruptive styles and can occur with little to no precursory signals (Barberi et al., 1992; Hurst et al., 2014). Styles can include phenomena such as ash columns - both large (~7000 m high at Mount Ontake in 2014: Kato et al., 2015) and small (~180 m high at Akita Yakeyama in 1997: Ohba et al., 2007) and crater formation (e.g. Inyo Craters, California: Mastin, 1991; Patom Crater, Russia: Antipin et al., 2015). When an overlying water body such as a crater lake is involved other phenomena are present. Dome-shaped bubbles above a lake surface have been noted at Lake Voui at Aoba volcano, Vanuatu in 1991 (Bulletin of the Global Volcanism Network, 1991) and Mount Usu, Japan (Okada, pers. comms). More explosive tephra jets and geyser-like eruptions are also recognised e.g. Mount Ruapehu, New Zealand in 1980 (Morrissey et al., 2010). The phreatic eruptive styles associated with bubble bursts, although mentioned in the above studies, have not been the subject of a detailed description before.

Controls on crater lakes levels are complex. Water mass balance determines whether a crater lake will grow or shrink at any given time (Brantley et al., 1993). Input of meteoric water by meltflow and precipitation (Hurst et al., 1991), and geothermal vapour or liquid (Trunk & Bernard, 2008; Werner et al., 2008) results in lake level rise. Decreases to the level occur through output processes of outflow, seepage, evaporation and boiling (Hurst et al., 1991; Brantley et al., 1993). Two mechanisms for lake boiling involve magmatic steam and transfer of heat from a magmatic source at depth to the lake vicinity via a heat-pipe structure (Hurst et al., 1991; Kasakube, 1996). Alongside these, volcanic tremor has been associated with both decreases and increases to crater lake levels at White Island (Werner et al., 2008; Chardot et al., 2015).

Frequent episodes of phreatic eruptions within a desiccated crater lake were recorded at White Island volcano, New Zealand during 2013. These were expressed as phreatic gas/steam bubble bursts in a mud-sulphur pool (hereafter simply referred to as a mud pool). Although hydrothermal activity has been recognised as common on White Island (Cole & Nairn, 1975) this style has not been previously described. We detail the observations of the first and longest phreatic episode from January 15 to February 7 at White Island, describing the distinct characteristics of the eruption style over this ~3 week episode. Additionally, we link the style during key periods with observations of physical changes to the mud pool and identify possible controls on the episode evolution.

2.3 White Island volcano

White Island, known also by the Māori name Whakaari, is an active volcanic island located in the Bay of Plenty, New Zealand, approximately 48km north of the coastline town of Whakatane (Figure 2.1). Volcanism here is driven by subduction of the Pacific Plate beneath the Australian Plate (Cole et al., 2000), the interface of which is expressed as the Hikurangi Trench ~200 km to the east. The volcano marks the southern end of a chain of seamounts forming the Tonga-Kermadec volcanic arc (Wright, 1992; Cole et al., 2000) and is the northernmost surface expression of the Taupo Volcanic Zone.

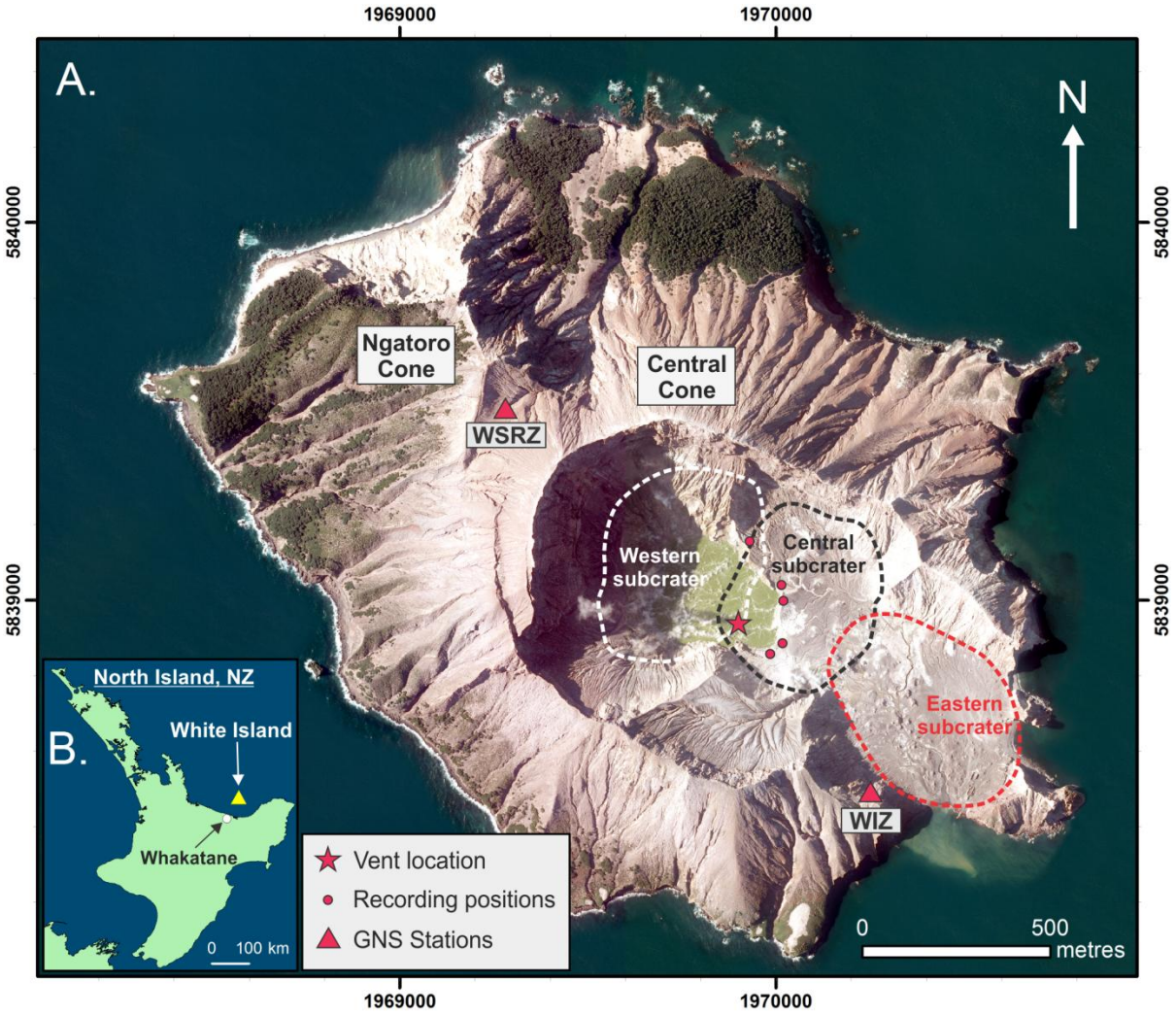

Figure 2.1: White Island volcano (A) with inset location within New Zealand (B). Subcraters are drawn from Moon et al. (2005).

Only the top 321 m of the larger White Island structure extends above sea level. The submarine section rises 300-400 m from the sea floor and covers a 16 x 18km area (Duncan, 1970). The subaerial structure spans 2 km (N-S) by 2.4 km (E-W) for a total area of ~3.3 km^2. This upper section consists of four cones - two overlapping composite cones, the extinct and eroded Ngatoro Cone, and the younger, active Central Cone (Black, 1970). Each is composed of andesite-dacite lava flows, agglomerates, tuffs, tephras, and breccias (Cole et al., 2000 and references therein).

A crater, named Main Crater, occupies a 0.4 km x 1.2 km area of the Central Cone. This is further subdivided into 3 subcraters - the Western, Centre and Eastern subcraters (Figure 2.1). All of the

historically active vents have been confined to the north-western side of Main Crater (Houghton and Nairn, 1991) with currently active vents limited to the Western subcrater (Werner et al., 2008). Unlithified tephra and volcaniclastic deposits (ash, tephra, lava, crater lake sediment and collapse debris) fill the Western subcrater to a depth of >250 m (Houghton & Nairn, 1989) with similar infilling predicted across the whole of Main Crater (Mongillo & Wood, 2000; Jolly et al., 2012). The crater lake currently occupies the Western subcrater.

Three breaches of the Central Cone to the southeast give White Island an amphitheatre-like shape. Large submarine debris fans to the east of the island indicate this current morphology is a result of a large ($2.1x10^8$ m^3) sector collapse (Cole et al., 2000; Moon et al., 2009). This collapse is thought to be a result of a telescoping porphyry and hydrothermal alteration, weakening crater walls to the point of failure (Sillitoe, 1994).

Historical eruptive activity has been dominated by phreatic and phreatomagmatic activity (Houghton & Nairn, 1991; Letham-Brake, 2013) with long periods of hydrothermal activity between eruptions (Cole and Nairn, 1975). A long established (>10ka) large volcano-hydrothermal system is present within the upper kilometre beneath Main Crater (Giggenbach and Glasby, 1977; Nishi et al., 1996). At the surface this expresses as fumaroles, hot springs, mud pools and an acidic crater lake and streams. These features are promoted as a tourist attraction, drawing >13,500 visitors annually (Letham-Brake, 2013).

2.4 Precursory and subsequent activity

From mid 2012 the lake level dropped significantly, drying from an expansive lake spanning the crater floor to form three isolated pools by the beginning of January 2013 (Figure 2.2). The largest of these pools, through which all of the 2013 phreatic activity occurred, formed in a similar area as the 1971 crater and was measured by GNS at 70-80°C on January 7. A cooler 30°C pool formed to the northeast, with the third pool containing a 20 m wide lava dome which formed at some point between August and November 2012 (GNS, 2013).

Periods of tremor were recorded prior to this near-complete drying. In both June and July 2012 strong tremor was noted, with elevated tremor between September and December (Chardot et al., 2015; Jolly et al., in review - Appendix A). An eruption occurred on August 4 2012, ejecting ash and blocks and continued through August as smaller mud eruptions (Chardot et al., 2015). These later mud eruptions were not consistently observed as strong degassing from the crater lake during this month obscures the majority of this activity.

Following the January/February episode, similar activity was observed during periods in late February, March, April, July, August and October 2013. Two larger eruptions, immediately prior to the August activity and following that of October, lasted ~1 and 10 minutes respectively and ejected large amounts of mud across the subcrater floors (GNS, 2013). No phreatic activity was recorded after the October eruption.

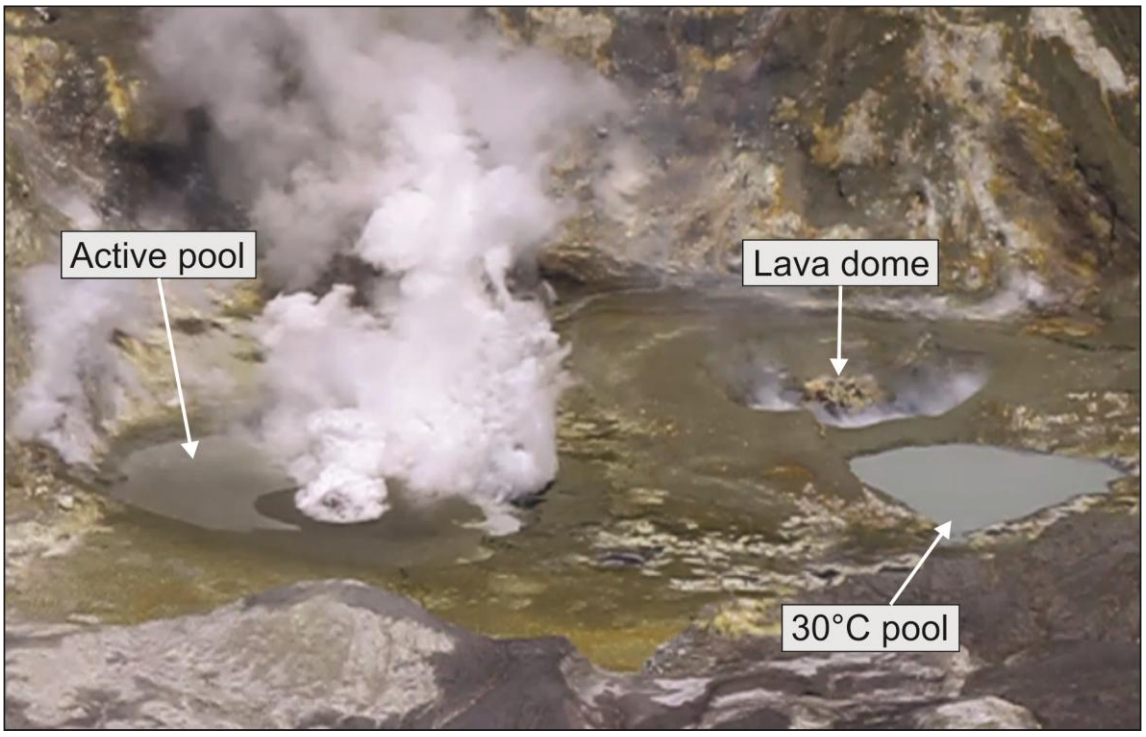

Figure 2.2: Crater lake condition on January 25 2013.

2.5 Method and datasets

Data in the form of video recordings and photographs were made available by tour operators and GeoNet staff. All recordings were taken by handheld cameras from 1 of 5 locations within the main crater (Figure 2.1) or during gas flight surveys. The majority of recordings took place from the two southern-most locations. Videos ranged in length from 8 to 186 seconds and were recorded at standard frame rates of 24 and 30 fps. Individual bursts were isolated from each video and separated into frames before being stabilised using a rigid body transformation via the ImageJ plugin StackReg (Thevenaz et al., 1998), or an inbuilt alignment script within Photoshop CS5. Manual tracking was performed via the ImageJ plugin MTrackJ (Abràmoff et al., 2004).

Maximum heave heights were measured from the video record. Heaves are defined here as the secondary upheaval or ejection of mud after a primary hemisphere formation or rapid gas jet, and produced by drag of an ascending bubble. The maximum heights generally correspond to heaves which disaggregate during ascent and eject in a near-vertical direction. Caution must be taken on the maximum heights (Figure 2.5) as measurements come from only the events preserved in the video record.

The separate scales used for each video were attained by calculating fall distances of any particle where a peak height was observed, using the equation:

$$h = \frac{1}{2}\, g\, t^2 + v_{(i)}$$

where h is vertical distance in metres, g is the gravitational constant (9.81 ms^{-2}), t is time in seconds, and $v_{(i)}$ is the initial velocity (0 ms^{-1} at the peak). The number of frames between a clast's peak (t_0) and lowest observed point (t_1) was timed (Figure 2.3-A). Particles were only analysed if they were observed to impact within 10 m of the burst origin in order to improve accuracy.

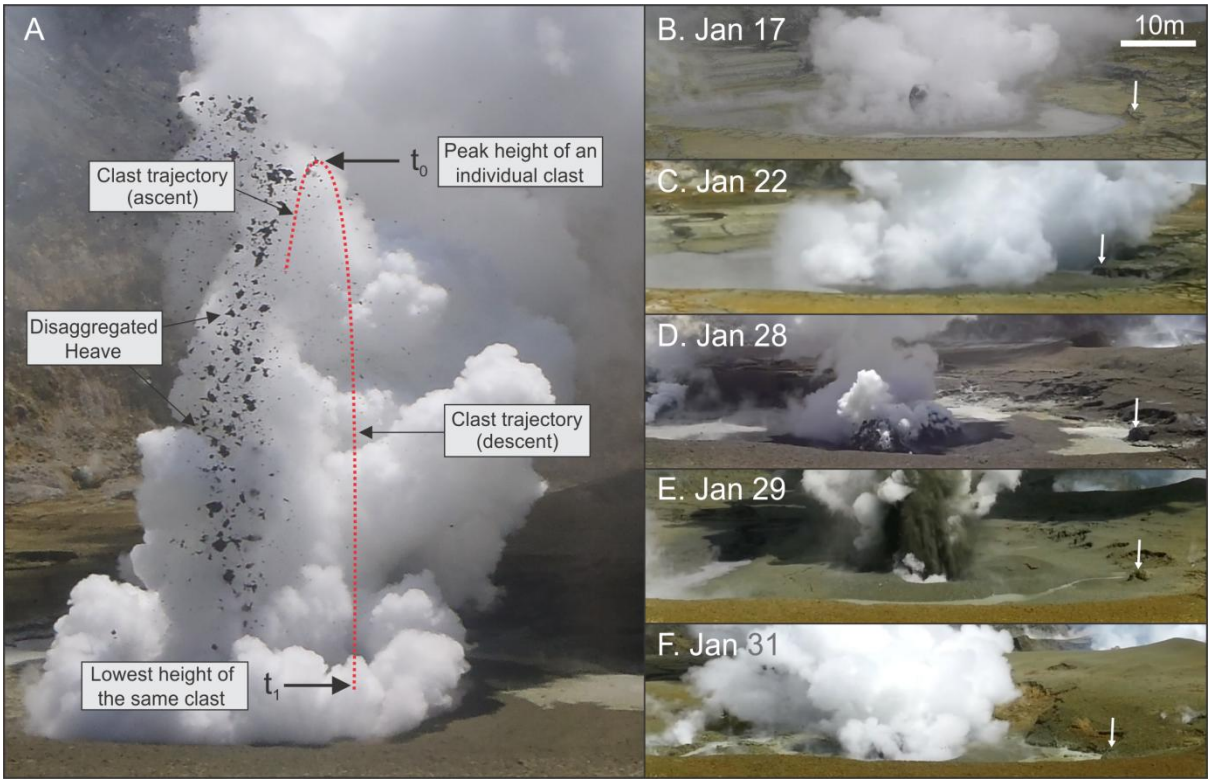

Figure 2.3: Example method of attaining scale (A), and common feature identification of outcropping terrace section (white arrows) for measuring lake level (B-F).

Lake levels across the episode were calculated by comparison heights of an exposed terrace section (Figure 2.3-B-F). This section extended into the pool in line with the centre of activity and represented the most clearly identifiable section for the majority of recordings. GNS methods for measuring lake height were not suitable for a highly desiccated lake so no data is available over the episode. The fixed GNS station WSRZ which has direct view of the pool was not installed until after the episode (Figure 2.1).

Seismic and acoustic data was recorded on a single permanent station (WIZ) which incorporated a Guralp 3ESP broadband seismometer and a co-located Setra 270-600 pressure transducer (Figure 2.1). Each was sampled at 100 hz on a Quanterra Q330 digitiser. Data was processed in the same method as Jolly et al. (in review - Appendix A).

2.6 Observations

2.6.1 Eruption regimes of January 15 to February 7

The episode of elevated activity varied in style between January 15 and February 7. Here we summarise the sequence through classification of activity styles into four distinct regimes (Figure 2.4), separated into key periods across the ~3 week period. The progression through these regimes appeared to correlate with a trend of increasing maximum heave height measured on each day (Figure 2.5), and changes in lake level (Figure 2.5). All activity occurred within the largest of the three pools.

January 15 to January 23. Dominated by the irregular bubbling Regime 1. It begins as irregularly-shaped mud hemispheres on the lake surface. These hemispheres collapse in place rather than explosively/energetically bursting and heaves produced eject in random directions. Highly fluidal strings of mud are produced during heave collapses (Figure 2.4-A) which fragment and rapidly contract into spherical clasts. Clast morphology becomes much clumpier and the string-like structures become less apparent by January 23 (Figure 2.4-C). The episode begins with heaves of ~8 m on January 15 and 16. Heave heights increase to ~38 m on January 21 and 22 (Figure 2.5). Bubbles produce an increasingly hemispheric shape at the surface as time progresses through this regime (Figure 2.4-B). The active pool remains at a relatively constant level between 15 and 23 January although an approximate pool level drop of 0.5 m occurs between January 17 and 18 (Figure 2.5). Different camera positions and obscuration by the gas/steam plume hinders precise measurements of the pool between days. Waves are visible following bubble bursts on the surface of the pool during Regime 1 (Figure 2.4A).

January 24 to January 25. Dominantly hemispherical bubble burst Regime 2. This period is characterised by the emergence and eventual dominance of a new eruption Regime 2, but also continuation and decline of bubbling Regime 1. Regime 2 is defined by bubbles that now produce very well-formed, highly symmetrical hemispheres of consistent 6 to 7 m diameter which burst explosively in what we describe as a 'starburst' event (Figure 2.4-D). This effect is produced by an

apparent brittle disaggregation of the hemisphere into similarly-sized angular mud clasts which are ejected in all directions away from the centre of the bubble. Starbursting is initially weak, with clasts maintaining their shape while being ejected <0.5 m. This starbursting becomes more explosively towards the end of January. A heave of mud, follows the larger burst events (Jolly et al., in review - Appendix A). Variation exists within heave size and timing in that they are either small enough to be contained within the hemisphere or erupt through the hemisphere prior to, or within 1 second of, the starburst event. Heaves increase in height b January 25 to a maximum of ~50 m (Figure 2.5).

January 26 to January 28. Emergence of a new burst/gas jet and mud heave Regime 3 which increases in frequency during this period, whilst Regime 2 remains dominant. Regime 3 is defined by the lack of any surface deformation (no hemispheres), instead producing a rapid, narrow gas jet at velocities of up to ~110 ms^{-1} (Figure 2.4-E). A burst associated with this jet is much smaller volume and less distinct in the video, ejecting generally finer <20 cm size clasts. Gas jet volumes are visually estimated to be greater than those exposed following starbursts of Regime 2. In all observations the burst and gas jet is followed by a directed heave (Figure 2.4-F). Direction of the heave is less variable than in Regimes 1 and 2, with many displaying a near vertical orientation, of which the greatest measured heights are reached of 102 m on January 28 (Figure 2.5). However, a significant horizontal component to direction emerges often with a distinct south orientation, landing on the terraces at distances of up to 32.4 m (Jolly et al., in review - Appendix A). Discolouration of the terraces by this heave deposition highlights the extent of the horizontal heaves in the absence of video recordings and confirms a varied orientation, from at least South to East. By January 28 common reference points show a further 0.5 to 1 m drop in the lake level since January 18 (Figures 2.3 and 2.5). Water visible during these days becomes confined to the outer edges of the pool by the formation of a shallow angle (<2°) mound around the centre of activity. Regime 2 hemispheres dimensions are unchanged at 6 to 7 m wide.

January 29 to January 30 (prior to 10am). Dry mud (ash) venting Regime 4. An ash venting phase where the lake in the immediate proximity of the vent appears completely dry on January 29 and the

mud surface appears desiccated. Heaves cease with the onset of Regime 4 on January 29. During this phase the ejected clasts appear to be completely devoid of all water which is associated with the larger clasts during the other regimes. Dry lake material in the ash fraction is ejected in a near constant venting with pulses every ~1 second (Figure 2.4-H). These pulse heights are consistently 60 to 65 m high and no sustained tephra plume is formed. Larger clasts are ejected which we assume to be lithics based on their size, colour and shape. The dry mud appears to coat a small tuff cone which is not directly visible during this episode but exposed in late February and March. Dry mud also deposits over the terraces surrounding the lake. At 10am January 30 pulse heights have decreased to ~30 to 40 m.

January 30 (after 1130am). Burst/gas jet and mud heaves of Regime 3. The venting phase has ceased and been replaced by burst/gas jet and heave events every ~1 to 3 seconds. This regression to Regime 3 by late morning on January 30 produces heaves of up to 27 m. Both burst/gas jet and mud heave are smaller than those earlier in January . Pool level is unable to be calculated however the bursts and heaves originate from approximately 2 m lower than the previous days. Heaved clasts are similar in size and shape as during Regime 3 events on January 26 to 28. Ejected mud associated with the burst includes mud clasts and the overlying dry mud. Water is only visible around the southern pool edge at this time. The absence of starbursts characteristic of Regime 2 at this time represents a key period not observed in the video record prior to ash venting.

January 31 to February 7. Starbursting and irregular bubbling Regimes 2 and 1. This period is bounded by the two regimes. Similar maximum height of ~26 m is measured during heave events associated with Regime 2 events on January 31. Absence of video within these days makes it unable to distinguish the exact boundary between regimes. By February 7 heaves are infrequent and reach less than 5 m high. Clast morphology reverts from an angular shape on January 31 to a highly fluidal shape on February 7. A near complete reestablishment of the pool occurs by February 7 (rise of ~1.5 m), but remains ~1.5 m lower than the level at the beginning of the episode on January 15 (Figure 2.5).

Although video recordings towards the end of February show an increase in phreatic activity, we consider the relative quiescence of February 7 as the end of the first eruptive cycle, moving into the second cycle afterwards.

Period / Date range	Regimes active	Clast morphology	Lake level change during period	Maximum Heave Heights (per day)	Seismo-acoustic characteristics
Jan 15 to Jan 23	1	Fluidal mud strings and rounded, spherical clasts. Loss of strings and clasts rounded but more elongate at episode end	-0.5m	7.9 to 36.4m	Weak - unidentifiable from noise
Jan 24 to Jan 25	1, 2	Clasts become more angular, similarly sized during starbursting.	No change	23.5 to 47.1m	N/A
Jan 26 to Jan 28	2, 3	Angular clasts of clumped mud during starbursting, and angular clasts of various size during burst and heaves of Regime 3.	-0.5 to -1.0m	39.3 to 102.3m	Regime 2 weak, Regime 3 strong
Jan 29 to Jan 30 (~10am)	4	Individual mud grains without any clumping evident. Larger angular lithics first seen.	N/A	33.8 to 67.0m	Weak to Moderate but sustained
Jan 30 (from ~11.30am)	3	Angular clumped clasts of varying size ejected by bursts and heaves. Finer dry mud ejected during gas jet.	-2.0m	19.7m	N/A
Jan 31 to Feb 7	2, 1	Angular clumped clasts during starbursting at beginning, mud strings at episode end.	+1.5m	25.2 to 4.8m	N/A

Table 2.1: Summary of the eruptive episode by key periods.

Figure 2.4: Regimes of the White Island phreatic mud eruptions. Regime 1 = A,B,C. Regime 2 = D. Regime 3 = E,F. Regime 4 = G.

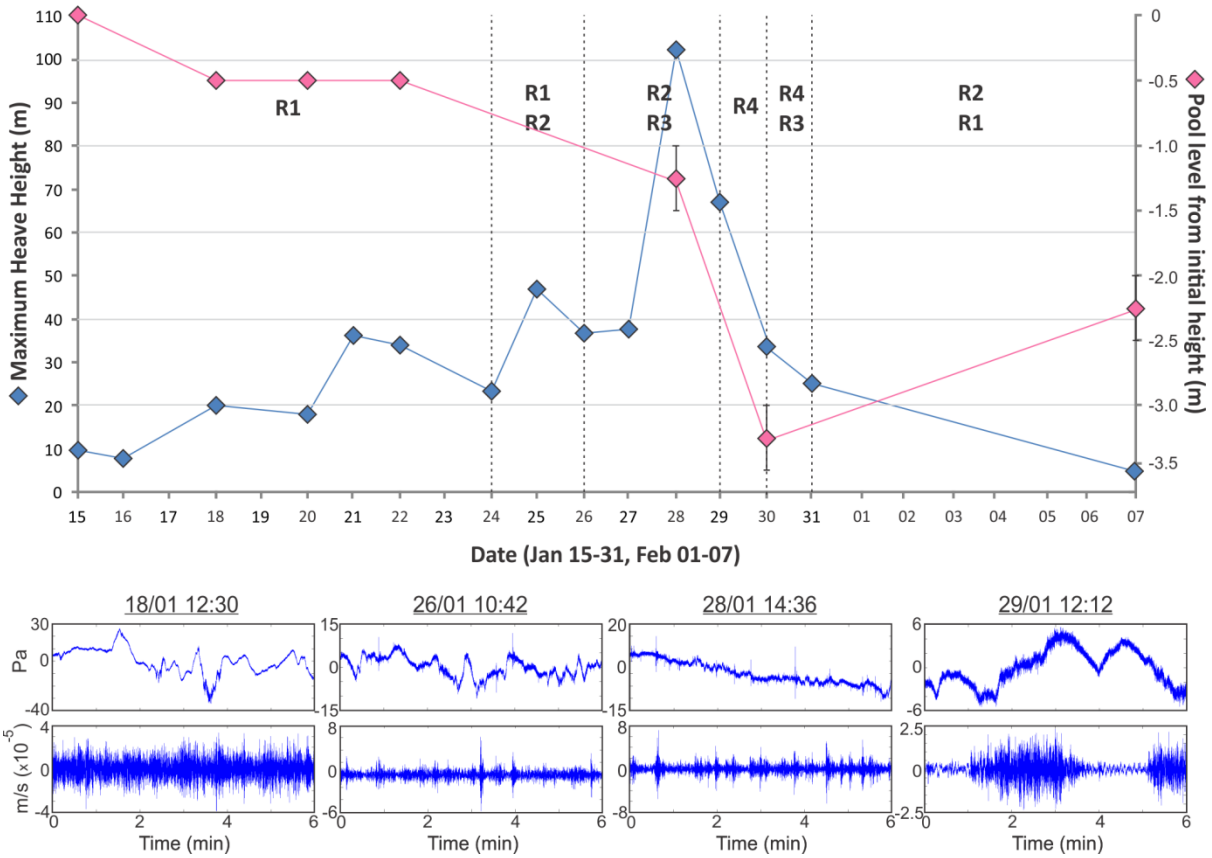

Figure 2.5: Maximum heave heights observed each day. Dotted vertical lines indicate boundaries of the key periods and onset of a new regime (R1-4). Characteristic acoustic and seismic profiles for each regime are shown below over a 6 minute period beginning at the title time.

2.6.2 Seismic and acoustic profiles

From the video record we identified individual dates and times when each of the four regimes were active or the most dominant during the progression. Seismic and acoustic profiles of 6 minute lengths around these times were produced to display the characteristic profiles of each regime (Figure 2.5).

Profiles for Regime 1 on January 18 show no strong features which can be interpreted as signal from the vent in either of the profiles. In this case we consider these to be entirely noise. Profiles for Regime 2 are also prove difficult to distinguish individual hemispheric starburst events. Peaks in these profiles are attributed to the concurrent Regime 3 burst, jet and heave events. Profiles for Regime 3

show an increase in these burst, jet and heave events. Peaks in the signals commonly match between the acoustic and seismic profiles. Profiles for Regime 4 show periods of weak to moderate sustained signal. The periods of quiescence within Regime 4 profiles are of unknown origin as these are not within video recording windows.

2.7 Discussion

2.7.1 Interpretation of evolving regimes

We attribute the progression through the various regimes to an increasing viscosity of the pool, shallowing bubble depth relative to the pool surface and an increase in the bubble/slug length in the conduit (Figures 2.6 and 2.7).

Increasing viscosity of the mud pool is likely a result of the loss of the water fraction by evaporation and boiling in proximity to bubbles. Further viscosity increases were achieved by the addition of material by erosion of the surrounding ash/lapilli terraces, observed to be caused by wave action during at least Regime 1. This helps to explain the relatively small changes in lake level prior to January 29. The clast morphology evolving from fluidal mud strings and spherical clasts to more solid, angular clasts of heaves and hemisphere collapse/burst also provides evidence for a viscosity increase. We also relate the ability of the increasingly symmetrical formation of hemispheres to viscosity increase. No material is observed to be lost from the mud pool by heaving during Regimes 1 and 2, some is however lost during horizontally-directed heaves of Regime 3. The highest heaves are near vertically oriented which results in the mud clasts landing back in the pool and a recycling of that material. It is not until the dry ash venting of Regime 4 when large amounts of mud are removed from the pool via wind-driven deposition on the crater floor. The fast re-establishment of this pool to the highly fluidal appearance of the beginning of the episode is a function of the lost dry mud of Regime

4. A smaller volume of water would have been required to achieve the same viscosity when the dry amount of mud was reduced.

An increase in viscosity is also supported by the seismic profiles (Figure 2.5). Peaks in signal of Regime 3 and 4 from January 26 indicate viscosity has increase sufficiently to support seismic waves, the support of which a fluidal pool would be incapable of.

A slug/bubble length increase must be occurring as well in order to produce the overall trend of increasing heave heights. Heave heights are shown to decrease with viscosity in mud analogue experiments when slug lengths remain the same (Thesis Chapter 3). With conduit dimensions at White Island constraining bubble width, any growth would result in slug-like bubbles. The lake level drop may also contribute to the increase in heave heights and is a factor we consider relevant for the evolution of Regime 1 while the pool remains fluidal.

The absence of any primary hemisphere during Regime 3 suggests a different bubble morphology during rise. A slow, consistent rise of spherical to slug-like bubbles is attributed to the primary hemisphere formations, with a faster ascending bubble tail due to pressure differences resulting in the secondary heave. The lack of a hemisphere therefore means that ascent of the slug was limited and specifically not able to slowly rise to the surface. Instead, we link this regime to the highest mud viscosities and suggest a brittle fracturing of the overlying mud resulted in depressurisation and release of the bubble volume at only a few metres depth. In this mechanism, a fracture propagates from the slug to the surface, creating a narrow pathway for gas escape. The width of this pathway has direct influence on the velocity of the gas jet - the same volume of gas through a smaller conduit results in higher velocities, providing an explanation for the fast 110 m/s gas jets. The burst of fine clasts associated with the gas jet are attributed to the widening of this pathway or ejection of the thin overlying mud as the fractures nears the surafe.

The fracture mechanism suggested fits in the observation of Regime 3 during the regression on January 30, however the occurrence of Regime 2 in conjunction with Regime 3 during January 26 to

28 requires further consideration. Variations in slug pressures and bubble length during this period may explain the different regimes. Gas overpressure is known to initiate fractures in unconsolidated material (Fauria & Rempel, 2011) and higher heaves are associated with longer slugs (Chapter 3). Evidence for these variations come from observations of plumes and heaves. The visual plume volumes following starbursts are visually less than that of the gas jets, and the heaves that follow starbursts are commonly small compared to the consistently high heaves after gas jets. Higher pressure short slugs and fracturing of the near-dry mud could therefore also be the mechanism for Regime 3 on January 30.

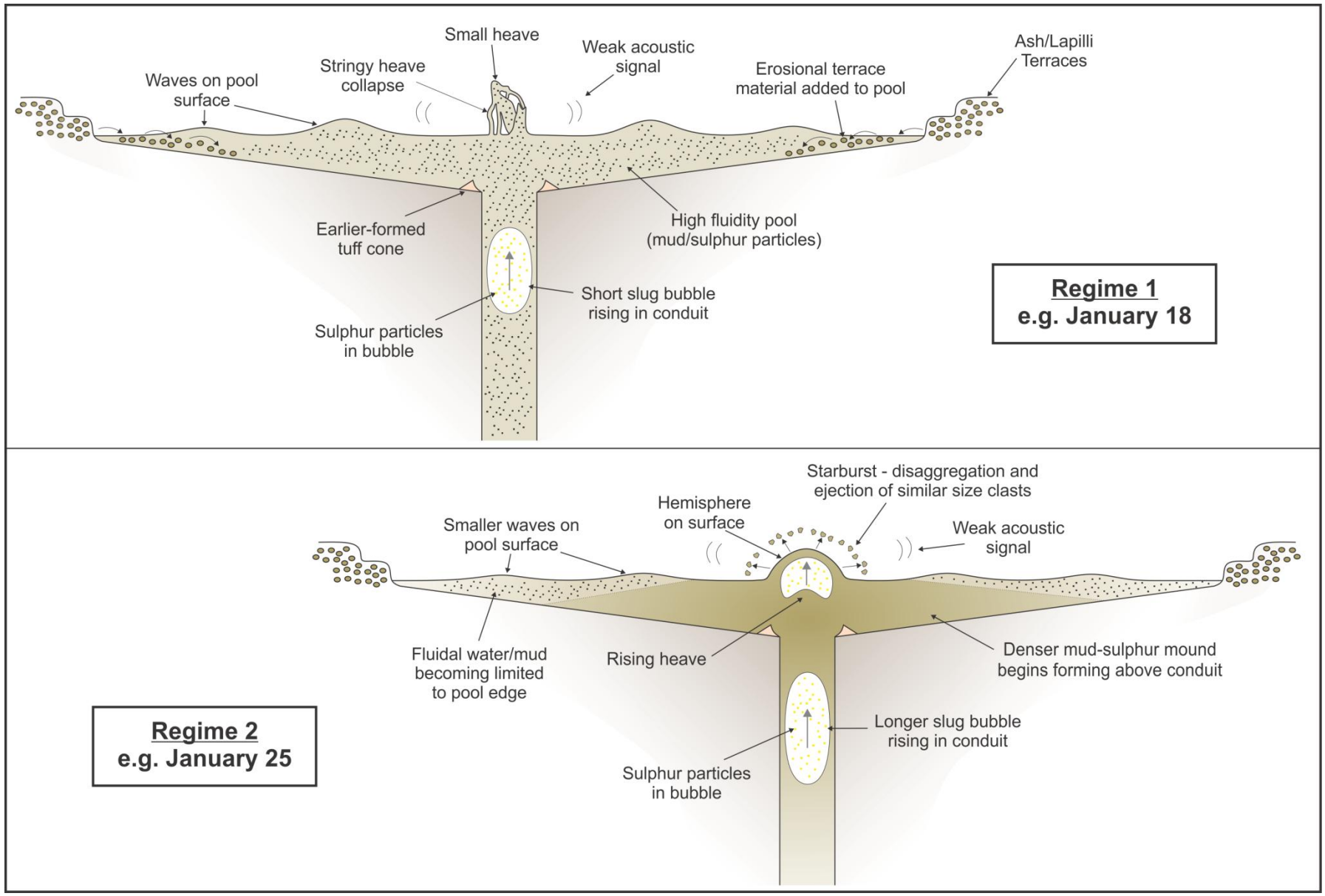

Figure 2.6: Cartoon depicting lake and bubble evolution during Regime 1 and Regime 2.

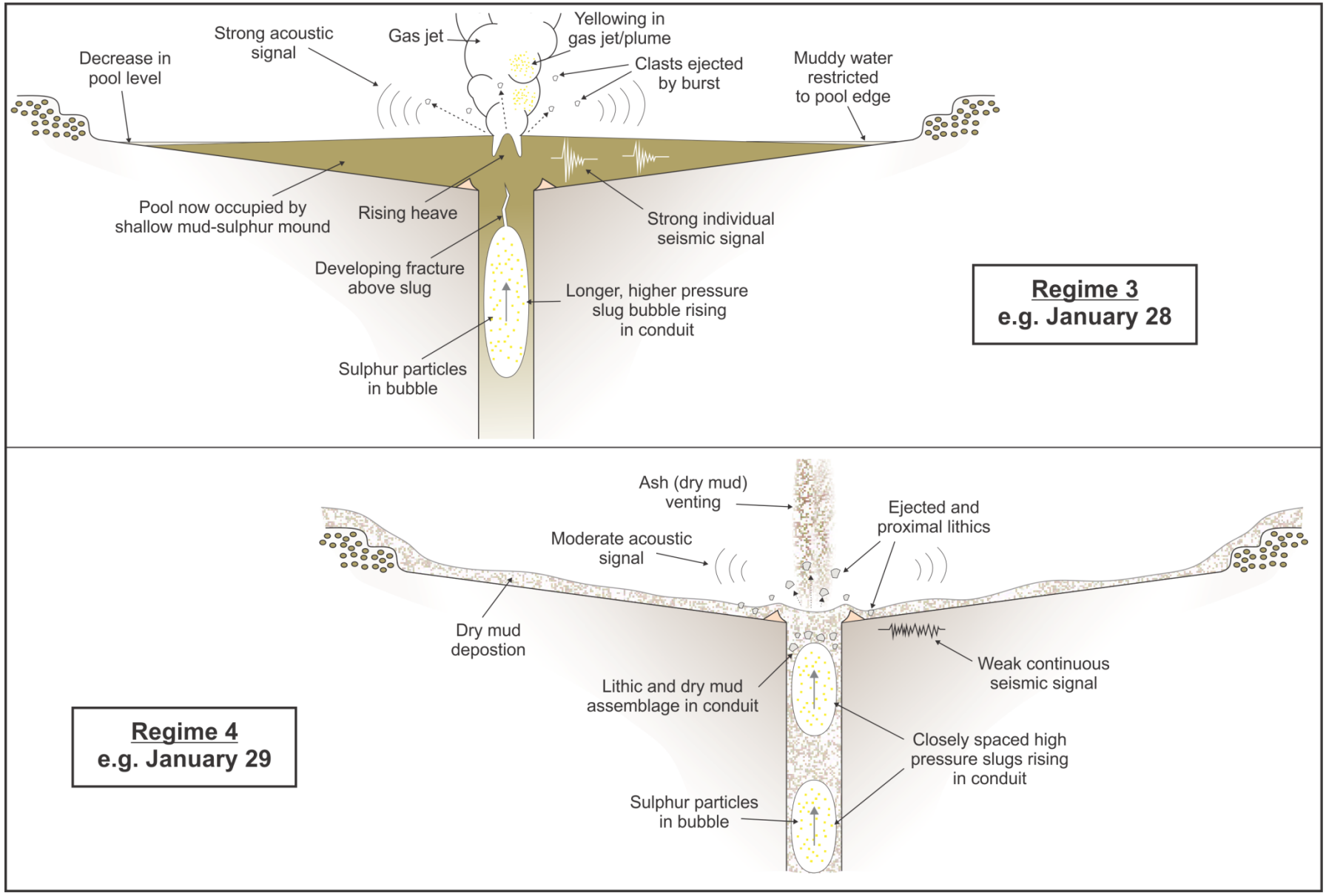

Figure 2.7: Cartoon depicting lake and bubble evolution during Regime 3 and Regime 4.

2.7.2 Phreatomagmatic or purely phreatic episode?

The presence of a magmatic component to the eruption sequence is discounted for several reasons. No juvenile ash was noted to be present by any GNS staff in this or any of the other similar mud eruption episodes later in the year. The best evidence for this is during the second episode at the end of February when the vent becomes completely clear of mud and no ash fraction is observed. Vigorous gas/steam venting is apparent from the exposed vent with no observed fallout and no discolouration indicative of a tephra component.

A distinct yellowing of the gas plume is clear at times in each regime but particularly with the exposure of gas/steam following the starbursts of Regime 2. This is an indication of a sulphur component however the grain size is too small to identify individual clasts in the video. A gas state is eliminated as a cause of this yellowing as SO_2 and H_2S are colourless gasses. Elemental sulphur can precipitate following condensation of magmatic-derived steam (Christenson & Wood, 1993) however the previously mentioned absence of ash limits this as a possibility during the episode. Accumulations of elemental sulphur at the bottom of crater lakes has been argued for at Mount Ruapehu (Giggenbach, 1974) and since shown to exist as a liquid layer at other volcanic crater lakes (Hurst et al., 1991 and references therein). We therefore consider the reheating and/or movement of sulphur at depth, as first described by GNS (2013), as a likely mechanism for the yellowing of the plume.

The overall desiccation of the crater lake between 2011 and 2013 has however been associated with intrusion and extrusion of shallow magma (Chardot et al., 2015). We suggest the desiccation of the active pool was a result of minor extensions of this intrusion, resulting in temporary increases to heat flux and impacting on the hydrothermal system (as in Cole et al., 2000). The complete desiccation of the pool on January 29 would therefore be credited to a peak heat flux, whereas subsequent cooling allowed water collection and re-establishment of the high-water fraction mud pool. Similar phreatic mud eruption episodes later in the year could therefore be attributed to further small intrusions. Although rainfall data is absent from White Island we exclude an increased water input as a factor for

lake reformation. No evidence of significant rainfall is apparent directly in the videos or through any large erosion features of the loose dry mud deposit following Regime 4.

2.7.3 Hazard implications for White Island and other volcanic/geothermal systems

A significant ballistic hazard arose within the studied episode towards the end of January. Hot mud clasts that were ejected during horizontally directed heaves impacted up to 32.4 m from their origin. Smaller clasts from bursts associated with the gas jets ejected greater distances before an unobserved impact. Despite this, tour companies operated without interruption. In quite the opposite, the activity was a drawcard for tourists in the peak of the New Zealand summer.

Although the episode of this study never increased in explosivity to a level where visitors were in danger, activity later in 2013 illustrated the hazard potential of phreatic eruptions. Similar regimes noted on July 26 had ceased on August 5, and after a period of quiescence within the mud pool a sustained 10 minute eruption of mud and steam of significantly greater size than the episode studied occurred on August 20 (GNS, 2013). Directional heaves were recorded by GNS webcams on October 8 of matching style but larger size of Regime 3, followed by a ~1 minute long eruption on October 11 (GNS, 2013). Daylight revealed fresh mud deposits across the entirety of the subcraters which would have been life threatening to anyone in these areas. With comparable precursory regimes it was reasonable to consider the possibility that this elevated activity might occur during January and February.

Similar eruptive styles as these White Island regimes can be seen at lava lakes (Bouche et al., 2010; Gerst et al., 2013; Ilanko et al., 2015), geysers (Namiki et al., 2014) and in strombolian eruptions (Lyons et al., 2010; Taddeucci et al., 2015). Evolving conditions at these may have the potential to produce similar eruptive styles as the later stage regimes. The effects of a drop in lake level of a geyser pool or lava lake, or cooling as a means of viscosity increase in lava lakes (Bouche et al., 2010) may induce a transition into regimes where ballistics becomes a hazard to visitors to the volcano or geothermal area. Periods of quiescence immediately following activity in crater lakes,

similar to those of August and October at White Island, should be of particular consideration. Heating of sulphur layers, common at the bottom of crater lakes, can block gas vapour from ascending, building pressure and increasingly the chance of explosive gas release (Hurst et al., 1991; Christenson & Wood, 1993).

The more explosive burst, gas jet and heave events of Regime 3 are easily identifiable in the seismo-acoustic record and represent another mechanism for hazard assessment. In periods when visibility of the activity is limited (e.g. obscured by a plume, outside of daylight hours, no real-time video monitoring) the record can be used to identify the presence of these most hazardous regime styles.

2.8 Conclusions

We describe an evolution of phreatic eruptions within a varying viscosity mud pool at White Island volcano over a ~three week period. The eruptive episode was persistently active and we observed both a progression of increasingly explosive eruption regimes prior to a dry mud venting phase, then a subsequent regression through the same regimes. Heave heights increased as viscosity of the mud pool increased, peaking on January 28 - the day before complete desiccation of the pool. The largest events of Regime 3 are recorded in the seismo-acoustic record and provide a method of hazard assessment in the absence of visual monitoring. A detailed analysis of slug bubble bursts in mud mediums has been undertaken to further link viscosity, slug length and burst depth to the White Island activity (Chapter 3).

Chapter 3. Experimental modelling of phreatic bursts

3.1 Introduction

Bubble and gas ascent is one of the key processes in a wide range of volcanic and geothermal activity. Significant variation exists though in the way these gases or bubbles manifest at the surface. Phreatic bursts triggered through the rapid expansion of water to steam have the potential to eject blocks on a km scale (Fitzgerald et al., 2014). Within lava lakes, bubble rise is attributed to dome formation on the surface at Villarica, Chile (Gurioli et al., 2008), Erta Ale, Ethiopia (Bouche et al., 2010) and Mount Erebus, Antarctica (Johnson et al., 2008; Gerst et al., 2013; Ilanko et al., 2015). Lava fountaining is also recognised at Erta Ale; attributed to the eruption of the bubbly wake of a larger near-spherical bubble (Bouche et al., 2010). Bubble ascent in magma can produce discrete, individual strombolian events, as at Stromboli (Blackburn et al., 1976; Vergniolle & Brandeis, 1996; Burton et al., 2007), Nyiragongo, Democratic Republic of Congo (Sawyer et al., 2008) and Kilauea, Hawai'i (Chouet et al., 2010; Edmonds & Gerlach, 2007) as well as fountaining hawaiian events, as at Etna (Ulivieri et al., 2013) and Kilauea (Jaupart & Vergniolle, 1989). Geysers are well linked to the rise of steam and water (Watson et al., 2014; Johnson et al., 2008; Namiki et al., 2014) and mud volcanoes at the Salton Sea, California are recognised to be a build-up of spatter from bubble bursts at a mud surface (Tran et al., 2015). In other volcanism, debris-filled vents at maar-diatreme volcanoes show evidence of gas and debris jets at depth (Ross & White, 2006).

Studies involving mud burst modelling are limited, however other research has been conducted on the similar driving mechanism of bubble ascent. In mud experiments by Tran et al. (2015) though bubble velocities during ascent in a mud-filled cylinder were shown to increase as bubble volume increased. Little effect was observed on these velocities when depth was varied. Strombolian and Hawaiian style volcanism has been investigated and linked to discrete slug rise and burst (Strombolian) and constant ascent of irregular bubbles to the surface (Hawaiian) (Jaupart & Vergniolle, 1988; James et al., 2004;

Pioli et al., 2012; Sánchez et al., 2014). Modelling of the debris jets of diatremes in granular material has produced surface doming and jet extrusion (Ross et al., 2008; Andrews et al., 2014). Of note is that this jet height decreases as initial depth increases; at certain depth a jet will not express at the surface. Geyser modelling shows vigorous boiling of water in an underlying chamber is necessary before slug vapour bubbles will rise to the surface and eject water (Saptadji, 1995; Adelstein et al., 2014). High pressure bubbles produced during underwater explosions have created 'upwards swelling' of water surfaces and large vertical water jets (Cole, 1948; Ichihara et al., 2009).

Bubble bursts at White Island share characteristics with most of these previous experiments but modelling requires special consideration of the variables. Single balloons simulate the discrete bursts observed in the video record, and are of shapes comparable to the bubbles which produce the strombolian eruptions and doming within lava lakes above. Different ratios simulate viscosity increases of the White Island mud pool as it dried. Various burst depths simulate decreases in mud pool level, and have further implications on heave height as per the noted diatreme and underwater modelling above. The two slug bubble lengths simulate possible growth of bubbles during the episode.

Results of these experiments are discussed within this chapter, and linked back to the White Island observations in the discussion of Chapter 4.

3.2 Methodology

All experiments were conducted at INGV, Rome during late February to early April 2015. The equipment set-up was designed to maintain consistency between experiments and consisted of:

- Memrecam HX6 high speed camera. Mud burst recordings were at 2000 fps at resolution of 1216x1284 px (maximum resolution possible for the frame rate and the best compromise for field of view). Recordings in water were at 1000 fps at resolution of 1920x2560 px.
- Optronis high speed camera. Recording at 500 fps at resolution of 800x600 px. Oriented at an angle down onto the tank surface, perpendicular to the HX6.
- Microphone (G.R.A.S. Type 26 HG) and amplifier
- Datalogger for cameras and microphone synchronisation
- Manual Trigger
- Laptops controlling the cameras and microphone
- Rectangular Glass Tank with internal dimensions of 28.5 cm (width 1) x 28.5 cm (width 2) x 49 cm (height). Total volume of 39.8 litres.
- Compressed air source attached to a curved aluminium pipe for balloon inflation

An image showing the set-up is given as Figure 3.1 with a simplified schematic of the electronic components in Figure 3.2. There were minor variations to the camera positions during experiments due to requiring to disassemble the set-up for weekend storage. For water bursts the HX6 was 260 cm from the tank centre, and 223 to 239 cm during mud bursts. The Optronis camera was 151 to 154 cm from the tank centre throughout. These differences are accounted for with different scales used for the equivalent burst analyses.

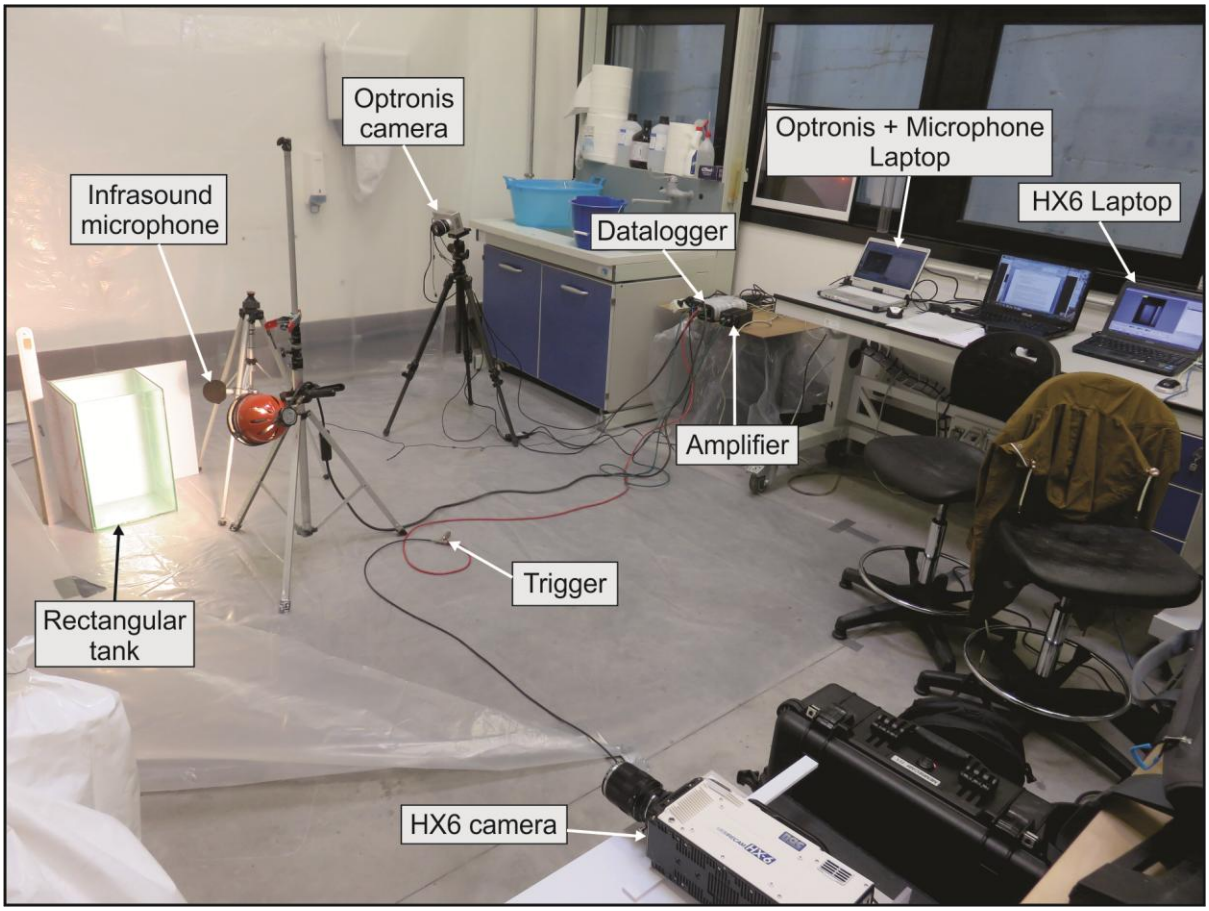

Figure 3.1: Experimental set-up at INGV, Rome.

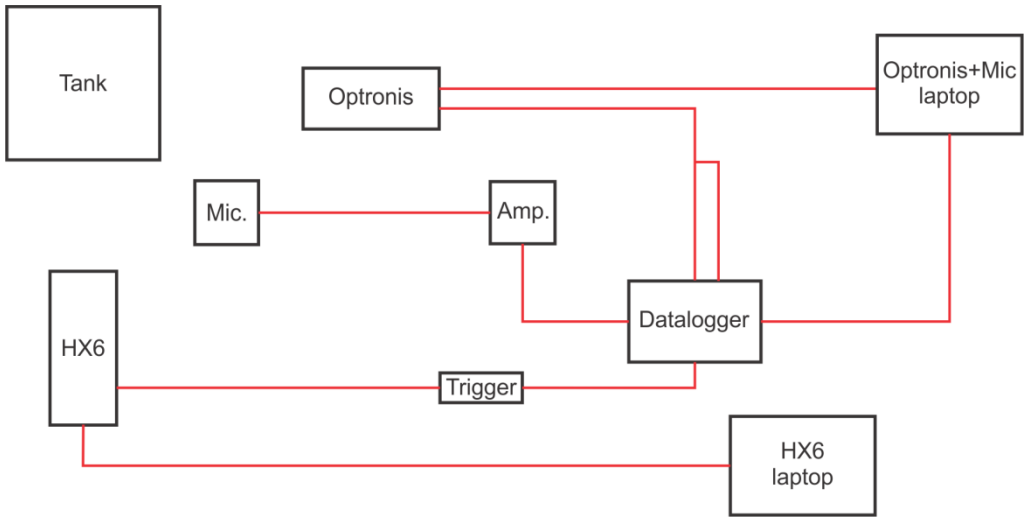

Figure 3.2: Simplified schematic of the electronic set-up with tank for reference (not to scale).

The glass tank was filled with various ratios of kaolinite powder to water (standard Rome tap water). These ratios were determined by mass, with measurements of each accurate to 1 gram. Mixes were combined by means of a paint mixing attachment on a power drill. Ratios were increased by addition of kaolinite powder to a known volume and ratio of the previous mix. A separate bucket was used to mix a reserve, which was used to re-level the tank after loss from balloon displacement and ejected material.

Kaolinite powder was used as an analogue to the White Island material as procuring a large amount from White Island was impractical (high risk during the eruption and inaccessible as the lake later re-established). Other material was tested at a smaller scale including soil and crushed marble but each was found to have a rapid settling rate. The settling rate of kaolinite powder was slow enough to be appropriate for experiments, with short remixing via the power drill if settling was observed.

Four different balloon shapes or lengths were used for experiments, named as Pear, Round, Slug (short) and Slug (long), based on their shape when inflated in air and shown submerged in Figure 3.3. The balloons were attached to an aluminium pipe containing the air source, by two cable ties secured on opposite sides to prevent leaking. Each balloon was inflated to the same length of 14 cm or 24 cm depending on the series. Inflation pressures were recorded by a manometer accurate to 0.01 bar. Pressures were similar within a single balloon shape, but varied between the 3 different shapes e.g. slug balloons inflated to the same pressure, but that value was overall higher than pressures for the pear balloons (Tables 3.2, 3.3 and 3.4). Widths of each balloon at their widest points when submerged in water type were consistent at 10 ± 0.2 cm for Round balloons, 8 ± 0.2 cm for Pear balloons, and 3.5 ± 0.2 cm for both Slug balloons.

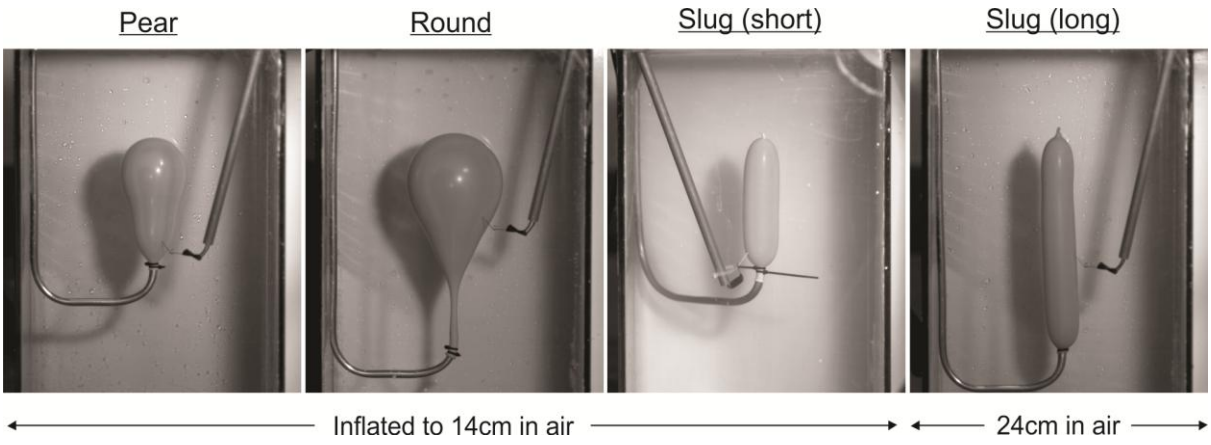

Figure 3.3: Example of each balloon type in water, submerged at a depth of 10cm.

Balloons were submerged as centrally as possible within the tank to depths of 0.5, 5 and 10 cm from the surface. The aluminium pipe (visible against the left edge of the tank in the images of Figure 3.3) was clamped to one wall of the glass tank in order to prevent movement of the balloon and to free up hands for operation of the other equipment. A pin angled upwards was attached to a separate metal rod (visible in each of the images of Figure 3.3) and used to burst the balloons. This mechanism prevented gas escape around the rod.

Two complete mixing sequences were done. The first sequence consisted of the 0.5, 0.75, 1.0, 1.2 and 1.4 ratios and Pear, Round and Slug (long) balloon experiments. The second sequence primarily consisted of 0.45, 0.6, 0.7 and 0.9 ratios and Pear, Round and Slug (short) experiments. This sequence was chosen after the first in order to both fill gaps in the first sequence and to link with related kaolinite powder:water experiments at LMU, Germany. The 0.5, 0.75 and 1.0 ratios were mixed again during the second sequence though and the Slug (short) balloon experiments performed for later comparison to the Slug (long) balloon. The Slug (long) balloon bursts, and mixing to 1.2 and 1.4 ratios for Slug (short) balloon experiments, were not performed during the second sequence due to time constraints. Pear and Round balloon bursts were attempted at all depths of the 9 ratios. The gaps (noted by 'X' in the figures within Chapter 3) for these balloons correspond to either difficulty in submerging balloons at the higher ratios, or partial/total absence of video through cropping error.

Both cameras began recording once balloons were submerged, activated manually via the laptops. Each constantly overwrote their internal memory buffer until the burst was observed and the trigger was pressed. When pressed a recording starting from ~1 to 2 seconds before the burst was saved and manually downloaded to the controlling laptop. Recordings were later exported as image sequences using the camera operation software. The higher quality images of the HX6 were ultimately used in all analyses.

Acoustic recordings began at the same time as activation of the Optronis camera. These recordings were not overwritten therefore ceased when manually deactivated on the laptop. Analysis of acoustics is not included in this thesis.

Particle tracking was done manually using the MTrackJ plugin in ImageJ (Abràmoff et al., 2004). The software Eject! was additionally used for heights where ejected material exceeded the field of view of the camera (Mastin, 2001). In these cases the average velocity of the last five tracking points, due to margin of error associated with manual tracking, was used as an initial velocity. The ejection angle was measurable within ImageJ. The height given by Eject! was added to the upper most height measured by tracking.

Rheology data was obtained using a Physica MCR 301 Rheometer. A vane attachment was used for each of the different ratios tested, with the amount of material for each ratio filling the cylinder to just above the vane. Twenty measurements were taken at each shear stress, with each taking 12 seconds. However, issues with cavitation at shear stresses high enough to overcome an initial yield stress of the ratios resulted in limited suitable data.

3.2.1 Sources of Error

Several sources of error are inherent within the experimental method, all of which contribute a level on variability to the sub-surface (in water) and surface manifestations (in mud). Error can be introduced through the experimental and analysis stages of balloon inflation, balloon depths, kaolinite powder and water mixing, and velocity tracking. The different sources of error are discussed below and quantified where possible.

Variation during inflation of balloons is created by differences in balloon length and inflation pressure. Consistent lengths of 14 and 24 cm were attempted however the inability to precisely measure length contributes at ±0.2 cm margin of error. Inflation pressure could not be controlled, the different pressures observed in the same balloon type and length is attributed to slight variation introduced during the balloon manufacturing process. The pressure within each balloon was accurate to 0.01 bar, with rounding of the manometer an error margin of ±0.005 bar is present in pressure measurements. Submersion depth of balloons was accurate to ±0.1 cm. Some difference in balloon orientation may be present but the effect of this is not quantified.

Kaolinite powder and water masses were measured accurate to 1g prior to each mixing. Error was created when increasing the ratio within the tank by addition of powder. Masses of the powder and water in the tank after balloon experiments when completed per ratio were calculated from the remaining volume. Error in measuring the mud height would result in incorrect addition of the powder. As height measurements were accurate to 0.1 cm the equivalent difference in ratio would be limited to < ±0.01 ratio at any given step. This creates a cumulative effect as higher ratios are reached through multiple mixings but maximum ratios remain accurate to ±0.03.

Velocity tracking and measurements from recordings were limited by the resolution of the camera. Direct measurements were therefore accurate to ±0.25 mm for all mud experiments and ±0.28 mm for all water experiments. For velocity tracking this corresponds to a ±0.28 m/s margin of error.

The cumulative effect of all of the described experimental sources of error are quantified by comparison of 3 repeated experiments involving the Pear balloon at the 1.0 ratio (Table 3.1). All results are assigned error margins based from these results. I consider percentage differences more appropriate than fixed cm values due to the range of bubble shapes and lengths used.

For 0.5 cm heaves the error margin is considered ±10.3%. I take a conservative approach towards the 5 and 10 cm heaves by assigning the larger margin of ±22.6% to both. The same approach is taken for all hemispheres with a ±11.2% margin regardless of balloon depth. Although these values appear high they typically relate to cm scale variations for all experimental measurements except the high heaves of 0.5 cm (Figure 3.7).

Depth (cm)	Heave Height 1 (cm)	Heave Height 2 (cm)	Heave Height Difference (%)	Hemisphere Diameter 1 (cm)	Hemisphere Diameter 2 (cm)	Hemisphere Diameter Difference (%)
0.5	24.8	29.9	**20.6**	9.9	8.6	**15.1**
5	9.9	10.8	**9.1**	13.9	13.8	**0.7**
10	4.2	6.1	**45.2**	15.9	13.9	**22.3**

Table 3.1: Uncertainties for mud bursts experiments. Based from repeated Pear balloon experiments at 1.0 ratio.

3.3 Experimental results

In this section I present results from all of the balloon bursts experiments. Particular focus is given to the heave event as this was a common feature measured throughout the White Island episode.

3.3.1 Bubble bursts in a water medium

Prior to the experiments within a mud medium, the same four balloon shapes were tested within a water-filled tank. This was done in order to visualise the changes to bubble morphology immediately after the balloon bursts, through to complete air escape at the surface. Such observations were not visible in mud as the addition of the kaolinite powder to water created an opaque mixture. Each balloon type was burst at each of the three depths examined. An overview of these 12 experiments is provided in Table 3.2.

Experiment Number	Balloon Type	Depth (cm)	P(air) (bar)	P(tank) (bar)	Length (cm)
39	Pear	0.5	0.1	0.1	14
40	Pear	5	0.09	0.09	14
41	Pear	10	0.08	0.09	14
25	Round	0.5	0.07	0.07	14
27	Round	5	0.07	0.07	14
28	Round	10	0.06	0.07	14
200	Slug (short)	0.5	0.13	0.13	14
199	Slug (short)	5	0.13	0.13	14
198	Slug (short)	10	0.12	0.12	14
33	Slug (long)	0.5	0.17	0.17	24
37	Slug (long)	5	0.14	0.14	24
35	Slug (long)	10	0.14	0.16	24

Table 3.2: Overview of all experiments conducted in water.

Bubbles performed similarly during ascent regardless of their initial shape. The change to bubble morphology can therefore be summarised into 6 steps:

1. Submerged balloons maintain their initial shape (Figure 3.4-A), apart from the Round balloon which develops a thin elongated tail caused by buoyant stretching. Balloon pressure increases by 0.01 bar to 0.02 bar (at 10 cm depth) (Table 3.2).
2. Immediately following the balloon rupture the bubble undergoes slight expansion then contraction (Figure 3.4-B). Edges of the bubble expand by up to 2.8 mm. The expansion results in a rapid apparent ascent of the head (Figure 3.5). A corresponding negative rise of the tail is visible in recordings but is not measured due to difficulty identifying the lowest point in each case (due to small bubbles obscuring the area). The related slowing of the tail as contraction ceases is identified in all but the Slug (short) balloon bursts though (Figure 3.5). This expansion and contraction is attributed to the bubble attempting to reach an equilibrium pressure.
3. The tail of the bubble begins accelerating towards the surface at a faster rate than the head (Figure 3.5). This effectively shortens the bubble with the air volume maintained by lateral expansion of the upper bubble half (Figure 3.4-C). The tail then slows as the bubble further shortens until a momentarily spherical shape is formed (Figure 3.4-D).
4. The faster moving tail continues to rise through the sphere - in particular the water being dragged by the tail penetrates the bubble and forms the beginning of a heave (Figure 3.5). An inverted-bowl shape bubble is created, appearing as a bubble with a rounded head and sides and a flat base from a side perspective (Figure 3.4-E). A rotational effect is observed where the bubble edges are seen to rotate downwards and in towards the heaving tail. A relatively steady rise of the bubble base occurs from this point (Figure 3.5).
5. The tail ascends/heave penetrates further and bursts through the rounded bubble head or hemisphere (Figure 3.4-F).

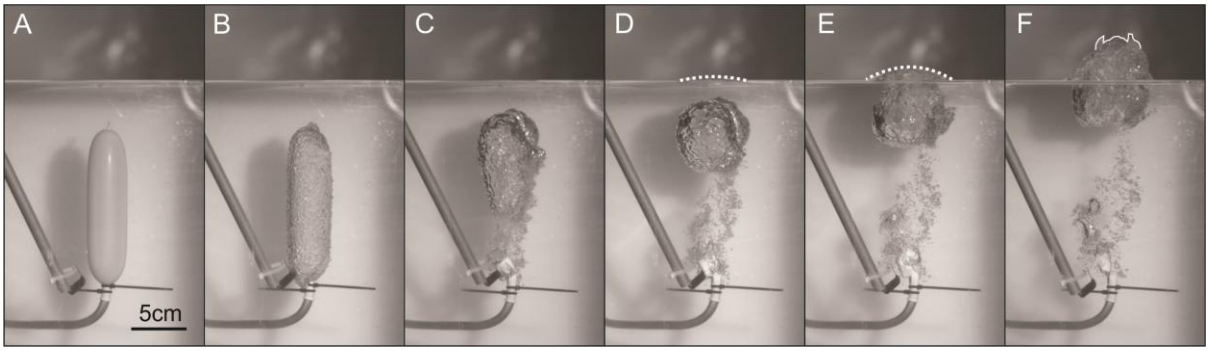

Figure 3.4: Example of bubble ascent in water - Slug (short) balloon at 5cm. A - initial submerged balloon, B - minor expansion following balloon rupture, C - bubble ascent and shortening, D - further shortening and sphericity with shallow hemisphere (dotted white line), E - inversion of tail with flat bubble base forming, F - hemisphere breach by heave (solid white line) and markedly flat base.

The same morphology change and processes occur in the slugs of increased length. The velocities differ however in that the tail overall moves much faster than the head prior to the overtaking phase (up to 4.5 - 6.5 m/s for 24 cm slugs vs 2.5 - 3.8 m/s for 14 cm slugs) (Figure 3.5). After this phase velocities are similar at ~0.5 - 1.5 m/s. Heave velocities are measured at a similar value of up to ~2.0 m/s once visible above the bubble head, and ascend at similar rates thereafter.

The initial balloon depth controls the depth at which the processes described above occur and the effect on the surface. At 5 mm the top of the bubble breaches the surface prior to the formation of a sphere. This burst ejects fine droplets and widens as air in the bubble is lost. The sphere and inversion occurs while the surface is breached. The tail is unrestricted and dragged water ejects through the surface breach.

At 5 cm the spherical bubble shape forms while still submerged (Figure 3.4-D). The tail/heave surpasses the head near the surface, ejecting water through a hemisphere produced by the bubble head (Figure 3.4-F).

At 10 cm, the tail overtakes the head of the bubble while still at sufficient depths that no hemisphere has yet formed. Surface features are therefore produced by the dragged water heave, having a more irregular morphology than the rounded hemispheres of the shallower balloons.

Plots of both the head and tail velocities show the variation present. The major features of the three 14 cm series are described together.

The expansion of the bubble causes a fast initial rise of the head at velocities of 0.7 - 1.8 m/s within the first 0.001 seconds (Figure 3.5). The expansion then decelerates for ~0.005s (up to ~0.017s for Round balloons) until no vertical rise is measurable. The head of the bubble remains stationary for 0.003 to 0.007s. From this point the head accelerates up to ~0.7 m/s, with some variation produced by minor distortion of the head surface. Ascent remains relatively stable at this velocity until breaching of the head by the tail at 0.7 - 0.9s. This tail accelerates towards the surface after the breach for approximately 0.015s at up to 2.0 m/s before slowing to 1.0 m/s. The breach of the tail is slower for the Round balloon, peaking at 1.0 m/s before slowing and appearing to increase again to ~1.4 m/s.

The tail accelerates steadily to a peak of 2.0 - 2.5 m/s after ~0.02 to 0.04s (Figure 3.5). The negative motion produced by bubble expansion is not measured due to uncertainty in the true tail position. The tail begins to slow as the bubble begins to become more spherical. The base velocity plateaus at 0.6 - 1.0 m/s as the tail protrudes and then breaches the head. For the Round balloon, an initial rapid acceleration in the first 0.04s is not clear from the tracking data.

Similar trends are observed when comparing the 14 and 24 cm Slug balloons however velocities are different (Figure 3.5). In general the tail moves faster, peaking at ~5.0 m/s (but possibly up to 6.4 m/s), before slowing to a similar 1.0 m/s plateau as the bubble base becomes flat (Figure 3.5). The head ascends at a similar rate as the 14 cm Slug, peaking at up to 2.0 m/s for the head breach by the tail, then slowing to 0.5 m/s, slower than the observable 1.0 m/s in the 14 cm Slug balloon.

The head velocities of bubbles from the 0.5 cm depth are not measured due to near-instant breaching of the water surface.

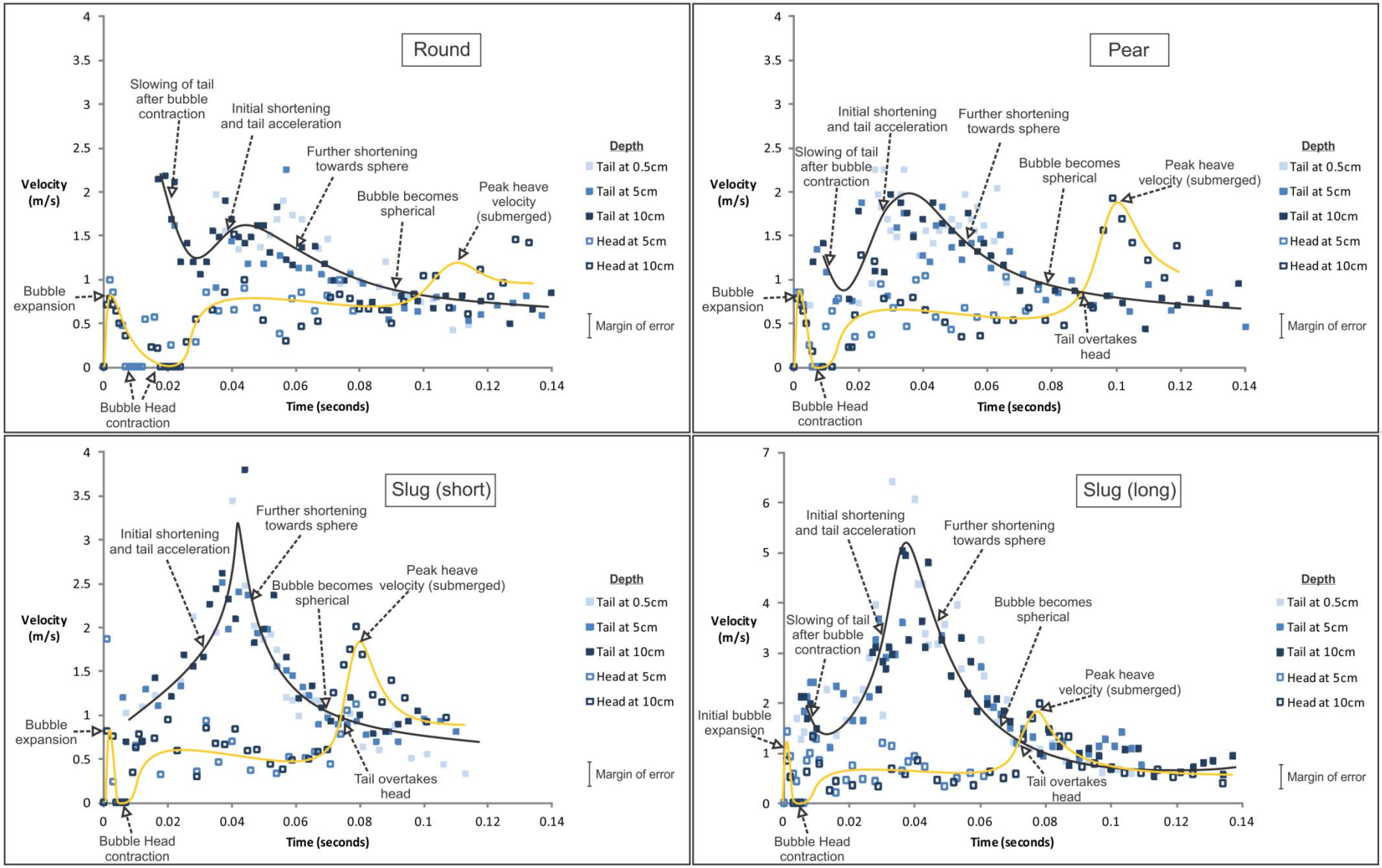

Figure 3.5: Bubble head and tail velocities during ascent in water for each balloon type and depth. Yellow and black lines approximate and illustrate the velocity trends of the bubble head and tail respectively.

3.3.2 Bubble bursts in a mud medium

Results of the mud experiments, conducted in the kaolinite powder:water mixes, are detailed in this section. Tables 3.3 and 3.4 show all the depths, ratios, pressures and balloon lengths for the given balloon types.

Balloon Type	Experiment Number	Ratio (Kao:H_2O)	Depth (cm)	P(air) (bar)	P(tank) (bar)	Length (cm)
Slug (short)	209	0.45	0.5	0.14	0.14	14
	208	0.45	5	0.11	11	
	207	0.45	10	0.13	0.14	
	221	0.5	0.5	0.13	0.13	
	220	0.5	5	0.14	0.14	
	219	0.5	10	0.14	0.14	
	227	0.6	0.5	0.14	0.14	
	226	0.6	5	0.1	0.1	
	225	0.6	10	0.14	0.14	
	245	0.7	0.5	0.13	0.13	
	244	0.7	5	0.12	0.13	
	243	0.7	10	0.12	0.12	
	260	0.75	0.5	0.13	0.13	
	259	0.75	5	0.14	0.14	
	258	0.75	10	0.14	0.14	
	266	0.9	0.5	0.13	0.13	
	265	0.9	5	0.13	0.13	
	264	0.9	10	0.14	0.14	
	285	1.0	0.5	0.14	0.14	
	286	1.0	5	0.12	0.12	
	287	1.0	10	0.14	0.14	
Slug (long)	86	0.5	0.5	0.13	0.13	14
	87	0.5	5	0.14	0.14	
	89	0.5	10	0.13	0.14	
	113	0.75	0.5	0.14	0.14	
	112	0.75	5	0.13	0.13	
	111	0.75	10	0.14	0.15	
	135	1.0	0.5	0.15	0.15	
	134	1.0	5	0.13	0.14	
	133	1.0	10	0.13	0.14	
	156	1.2	0.5	0.13	0.13	
	155	1.2	5	0.14	0.15	
	154	1.2	10	0.1	0.12	
	172	1.4	0.5	0.14	0.14	
	173	1.4	5	0.14	0.14	
	174	1.4	10	0.14	0.15	
Slug (length test)	281	0.9	5	0.15	0.16	25
	282	0.9	5	0.14	0.15	20
	283	0.9	5	0.14	0.14	18
	284	0.9	5	0.14	0.14	16

Table 3.3: Overview of all Slug balloon experiments in mud.

Balloon Type	Experiment Number	Ratio (Kao:H_2O)	Depth (cm)	P(air) (bar)	P(tank) (bar)	Length (cm)
Pear	203	0.45	0.5	0.07	0.07	14
	202	0.45	5	0.07	0.08	
	201	0.45	10	0.07	0.08	
	80	0.5	0.5	0.08	0.08	
	81	0.5	5	0.08	0.08	
	82	0.5	10	0.06	0.07	
	224	0.6	0.5	0.08	0.08	
	223	0.6	5	0.07	0.08	
	222	0.6	10	0.08	0.09	
	242	0.7	0.5	0.08	0.08	
	241	0.7	5	0.09	0.09	
	240	0.7	10	0.08	0.09	
	105	0.75	0.5	0.07	0.07	
	104	0.75	5	0.09	0.09	
	103	0.75	10	0.07	0.07	
	263	0.9	0.5	0.07	0.07	
	262	0.9	5	0.08	0.08	
	261	0.9	10	0.06	0.06	
	129	1.0	0.5	0.06	0.06	
	126	1.0	5	0.06	0.06	
	128	1.0	10	0.06	0.07	
	152	1.2	0.5	0.07	0.07	
	149	1.2	5	0.07	0.08	
	150	1.2	10	0.06	0.07	
	168	1.4	0.5	0.07	0.07	
Round	206	0.45	0.5	0.07	0.07	14
	204	0.45	5	0.07	0.08	
	205	0.45	10	0.07	0.08	
	84	0.5	0.5	0.07	0.07	
	85	0.5	5	0.07	0.07	
	85a	0.5	10	0.07	0.08	
	230	0.6	0.5	0.08	0.08	
	229	0.6	5	0.08	0.08	
	228	0.6	10	0.07	0.08	
	248	0.7	0.5	0.08	0.08	
	247	0.7	5	0.07	0.07	
	246	0.7	10	0.07	0.08	
	109	0.75	0.5	0.07	0.07	
	107	0.75	5	0.06	0.07	
	108	0.75	10	0.06	0.07	
	280	0.9	0.5	0.08	0.08	
	279	0.9	5	0.08	0.08	
	278	0.9	10	0.08	0.09	
	131	1.0	0.5	0.07	0.07	
	130	1.0	5	0.07	0.08	
	159	1.2	0.5	0.06	0.06	
	158	1.2	5	0.06	0.06	
	170	1.4	0.5	0.08	0.08	

Table 3.4: Overview of all Pear and Round balloon experiments in mud.

3.3.2.1 **Heave heights**

The maximum height of each of the 88 mud experiments were measured (Figures 3.6 and 3.7). Two general trends are observed in each of the three 14 cm balloon series.

Firstly, as the ratio of kaolinite powder to water increases (associated with viscosity increase) the maximum heave height achieved decreases. Maximum heights of 0.7 - 0.75 m are observed for the Pear and Slug (short) balloon series, with lower 0.4 - 0.45 heights in the Round balloon series. At ratio 1.2 heave height is typically minimal at <5 cm, and no heaves are produced at higher ratios.

There are two exemptions to this first trend:

- The Slug (short) balloons have an initial increase in heave height at the lower ratios (0.45 to 0.7), which is followed by a decrease thereafter.
- At the 1.2 ratio, a thin heave is produced at the 10 cm depth for the pear balloon, which is also seen in the Slug (long) balloons.

Secondly, there is a strong relationship between initial balloon depth and heave heights. Apart from the above exemptions, the maximum heave heights for any given depth and ratio are produced by the shallowest (0.5 cm) balloons. The reverse is also seen with the deepest (10 cm) balloons producing the lowest height heaves per ratio.

Comparison between the different slug lengths show substantial heave height increases when balloon length is increased. At the ratios directly comparable (0.5, 0.75, 1.0) Slug (long) balloon heave heights are 1.5 - 2.1 m higher than those of the Slug (short) balloon at 0.5 cm depth. This height variation is observed at the other two depths however is smaller at differences of up to 45 cm.

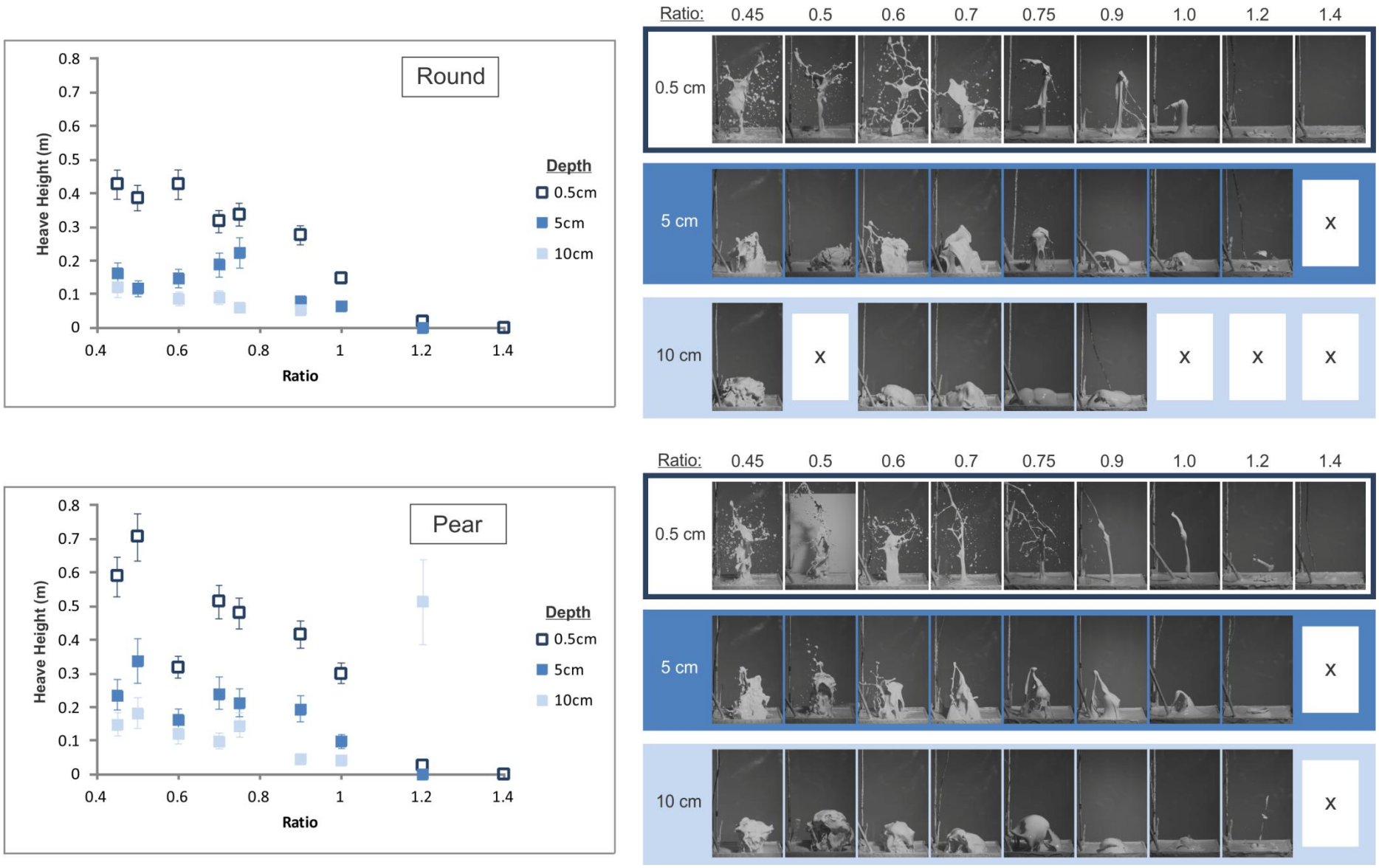

Figure 3.6: Maximum heave height for the Round (top) and Pear (bottom) balloon series at all tested ratios and depths, shown also as pictures to the right of each graph.

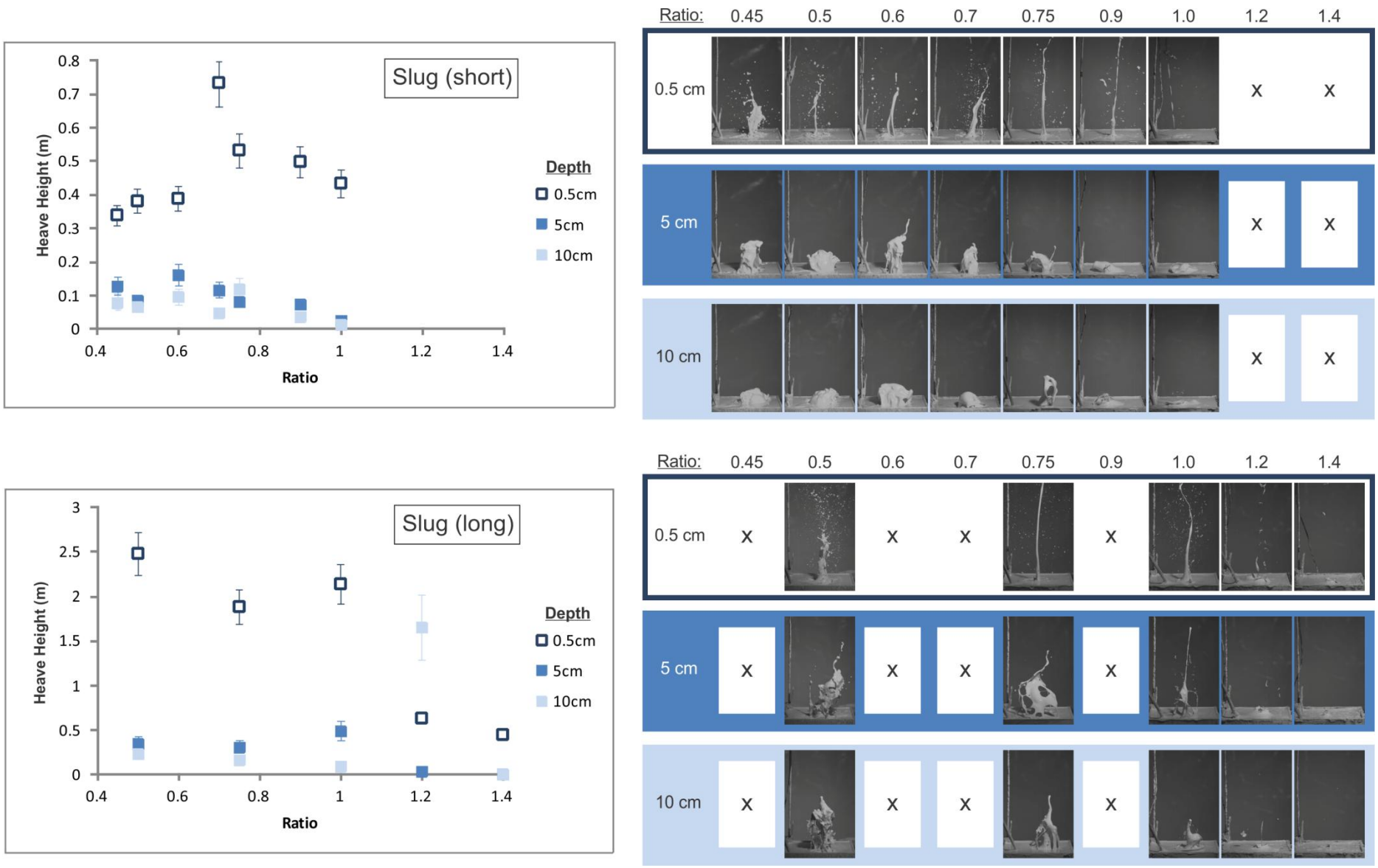

Figure 3.7: Maximum heave height for Slug (short) (top) and Slug (long) (bottom) balloon series at all tested ratios and depths, shown also as pictures to the right of each graph.

3.3.2.2 **Slug length control**

As well as the overlapping experiments of the two slug lengths at 0.5, 0.75 and 1.0 ratios, five experiments were done with a series of slug lengths at the 0.9 ratio at a 5 cm depth. In addition to the 14 cm slug at this depth and ratio, slug balloons were also tested at inflated lengths in air of 16, 18, 20 and 25 cm. Images of the maximum heights are displayed and graphed in Figure 3.8.

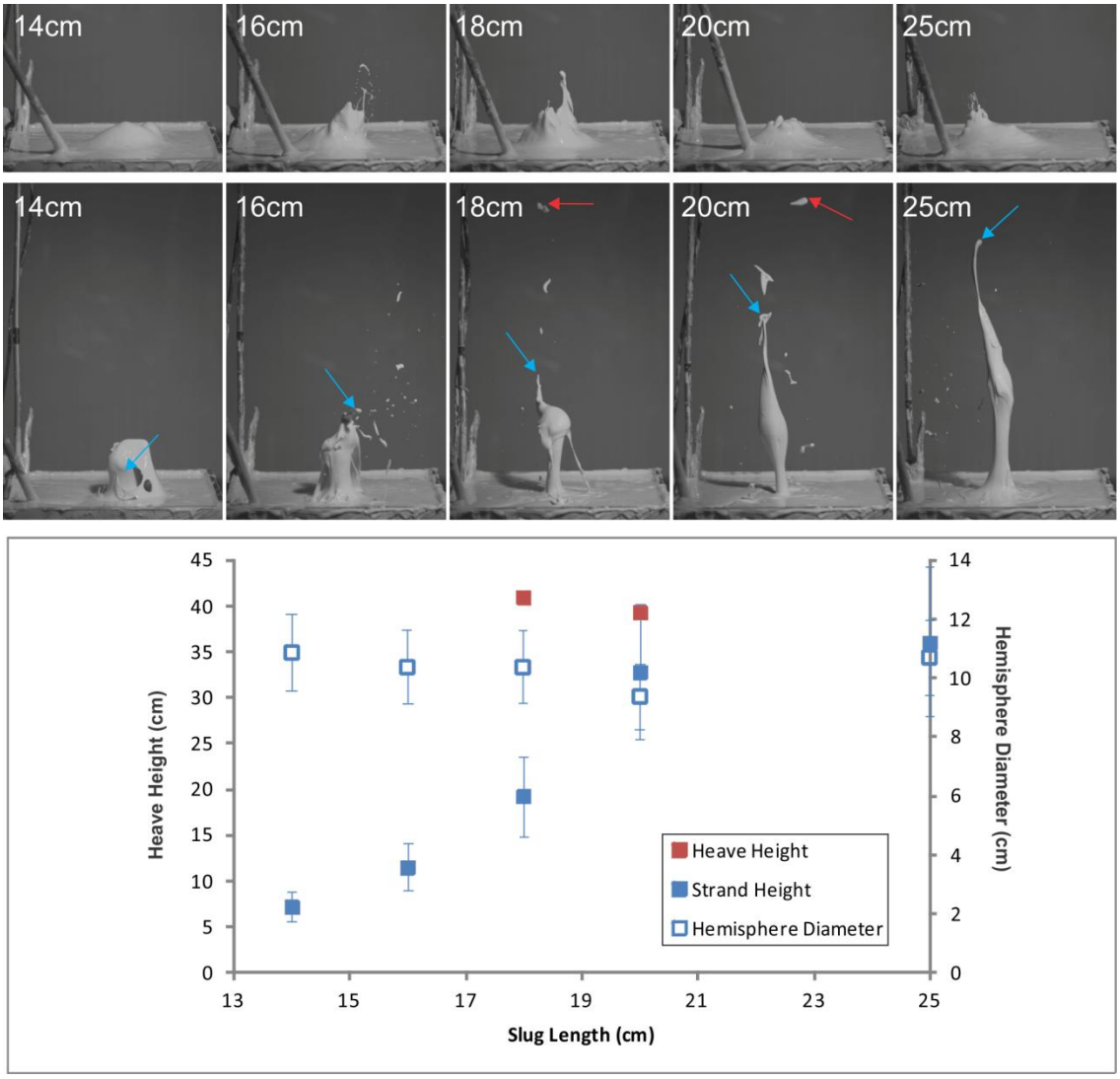

Figure 3.8: Heave height relationship with slug length at 0.9 ratio and 5 cm depth. Blue arrows indicate maximum strand height, where heave ascent has ceased but remains connected. Red arrows indicate maximum height of clasts which separated from the string during ascent. Arrow colours correspond with graph colours.

In fitting with the trends from the short and long slugs, an increase in heave height results from each increase in slug length, when no disaggregation of the top of the heave occurs. Where this separation does occur, as in the 18 and 20 cm Slug balloons, heights exceeding 35 cm are reached. The fragments visible in the 16 cm example were produced by bursting of a primary hemisphere.

3.3.2.3 **Hemisphere diameters**

Maximum hemisphere diameter for each experiment was measured prior to hemisphere collapse by bursting or penetration by the heave (Figures 3.9 and 3.10). There is no clear increase or decrease to hemisphere diameter as ratios increase. Instead, diameters are relatively consistent at depths of 5 and 10 cm for the individual balloon types. Hemispheres at this depth directly relate to the initial balloon width, with Round balloons producing the widest hemispheres of up to 22 cm, and both Slug balloons producing the narrowest at <15 cm.

Variability exists in individual balloon series at the 0.5 cm depth. The Round balloon at this depth has a ~10 cm range in hemisphere diameter, with smaller ~5 cm variations in the Pear, Slug (short) and Slug (long) balloons.

A consistent decrease in diameters is seen in all balloon types at the highest ratio of 1.4. Slug (long) balloon hemispheres are <6 cm wide at all three depths. Where other balloons were able to be tested at this ratio, diameters also do not exceed 6 cm.

Hemispheres which form from the 0.5 cm depth experiments rapidly burst at ratios of ~0.75 and lower. The minor upwelling prior to this is still considered hemispheric and therefore measured as such. At higher viscosities of ~0.9 and above hemispheres grow well above the surface before collapse.

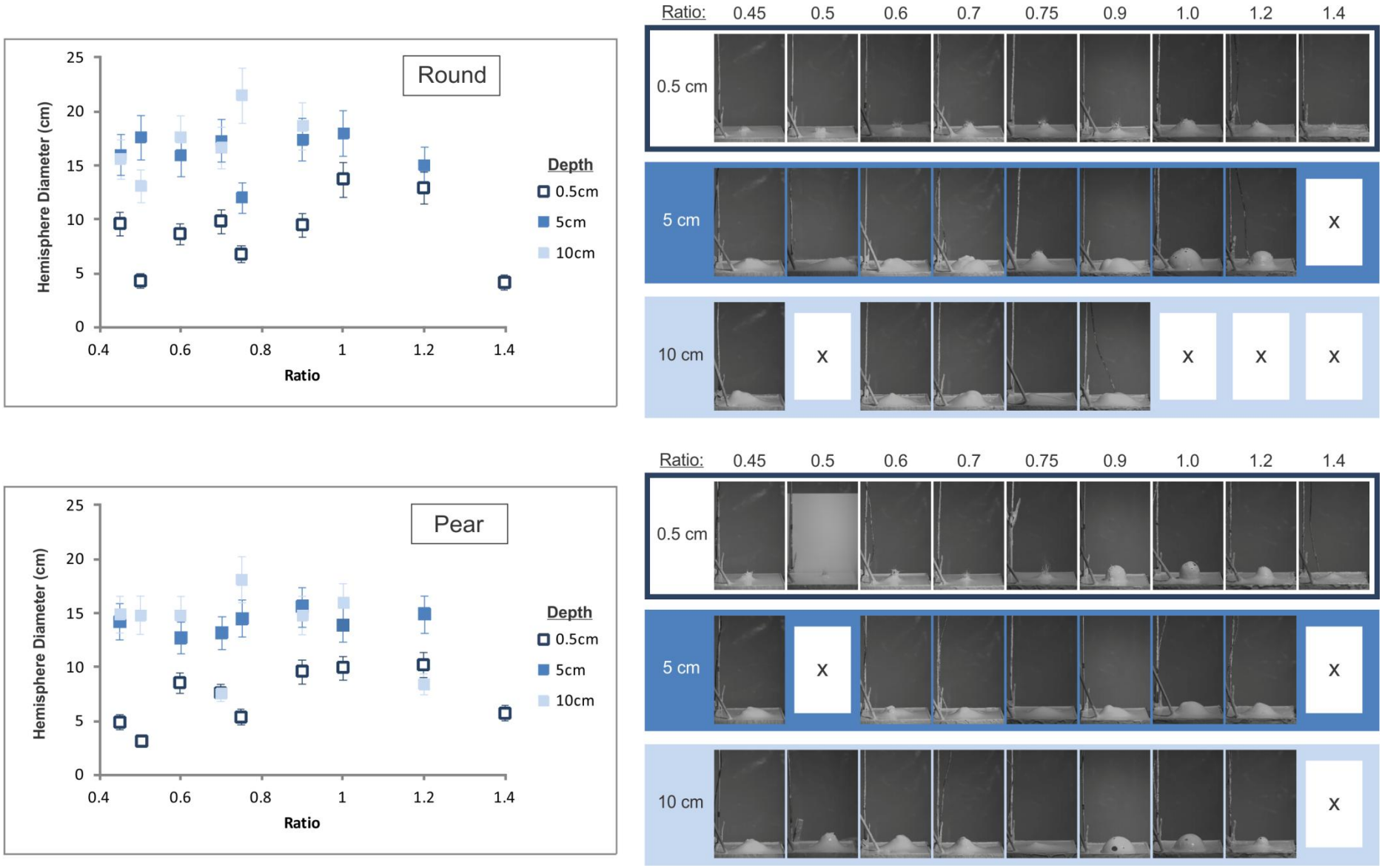

Figure 3.9: Hemisphere diameters for Round and Pear balloon series at all tested ratios and depths. Images to the right show immediately after hemisphere burst or sign of heave penetration.

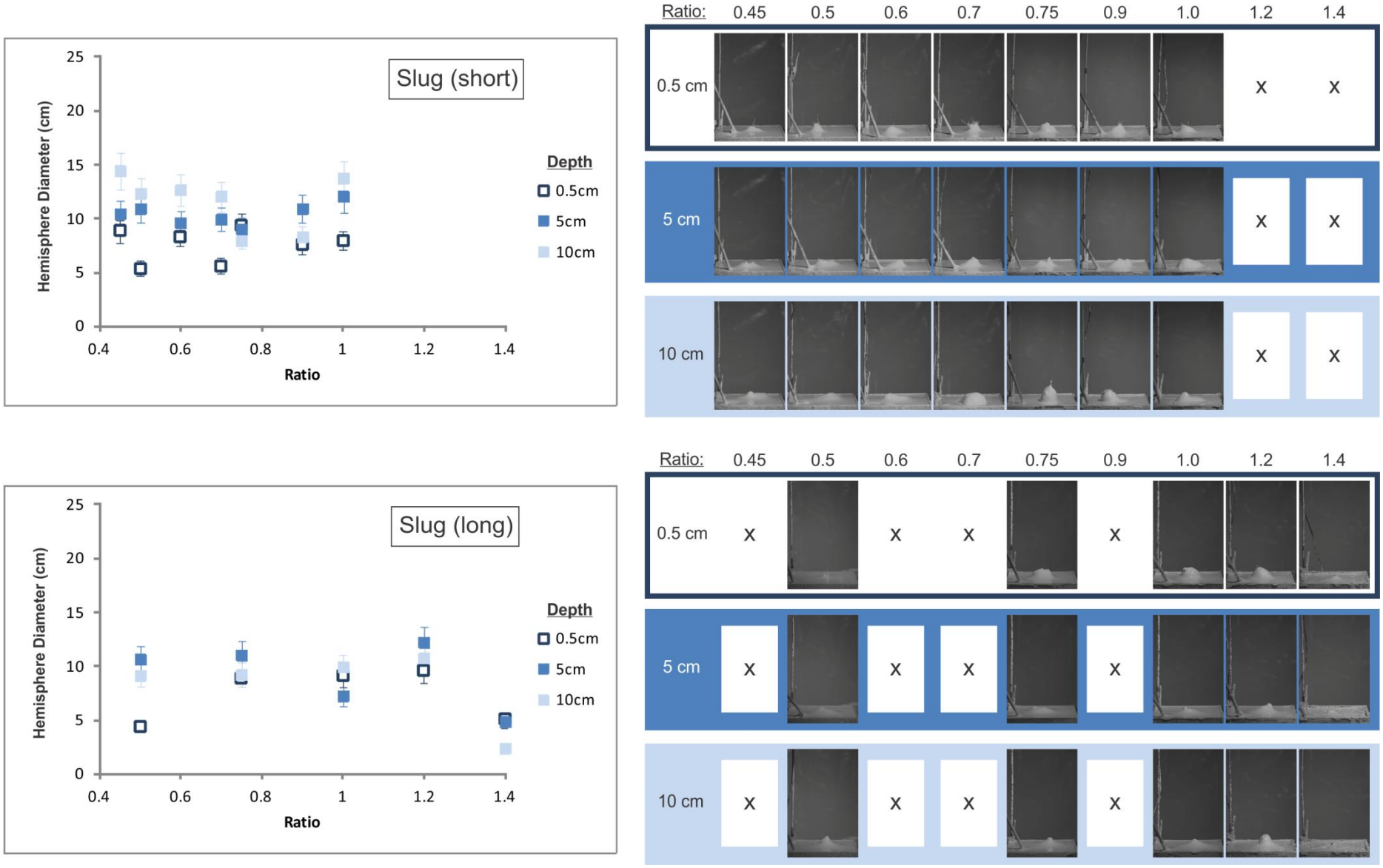

Figure 3.10: Hemisphere diameters for Slug (short) and Slug (long) balloon series at all tested ratios and depths. Images to the right show immediately after hemisphere burst or sign of heave penetration.

As with heave height, the initial balloon depth appears to influence the hemisphere formation. For any given ratio generally the smallest hemispheres are associated with the shallow 0.5 cm balloons, while the largest hemispheres correspond with the deepest 10 cm balloons. Some overlap exists particularly between the 5 and 10 cm depths but these are consistently larger than the shallow balloons.

Conversely, the Slug (long) balloon produces the largest hemispheres in four of the five tested ratios at the 5 cm initial depth. Diameters are similar for depths of 0.5 and 10 cm at the 0.75, 1.0 and 1.2 ratios.

By comparing hemisphere diameter with heave height, and independent of viscosity, the above trends can be summarised (Figure 3.11). Heave height has an inverse relationship to hemisphere size.

Points cluster based on depth showing small hemispheres and high heaves for shallow balloons, and large hemispheres and low heaves for deeper balloons. The plots where hemispheres size is small and heave height is low relate to the tests at high ratios of 1.2 and/or 1.4.

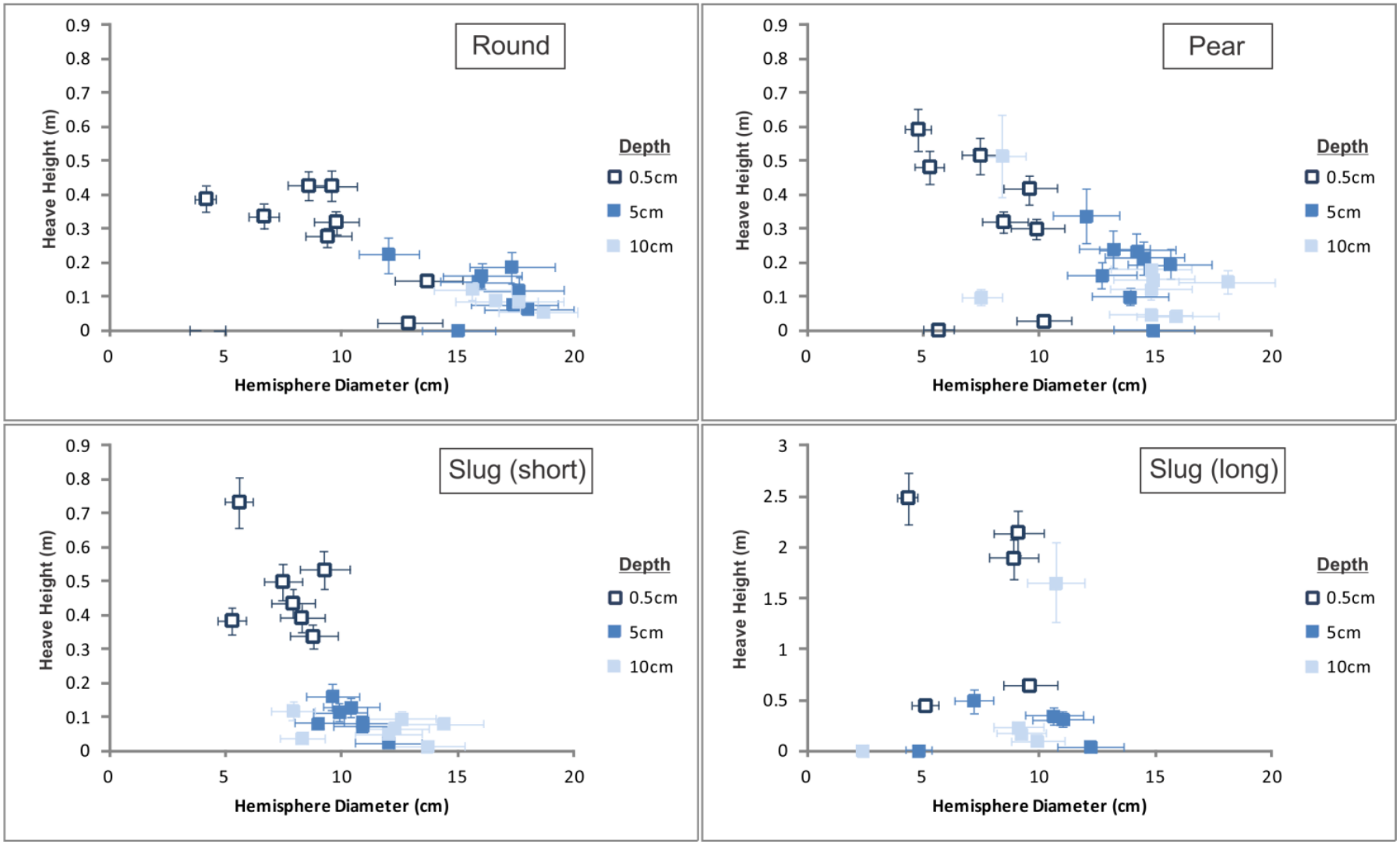

Figure 3.11: Heave height relationship with hemisphere size.

3.3.2.4 **Hemisphere collapse - burst or heave controlled?**

This section examines whether hemispheres that form on the mud surface collapse by bursting (burst controlled) or collapse when penetrated by a heave (heave controlled). For each of the four balloon types in the mud experiments, the control on collapse is identified (Figure 3.12).

At shallow depth of 0.5 cm, typically the hemisphere that forms on the surface rapidly bursts (Figures 3.9, 3.10, 3.12). In doing so, the upper part of the hemisphere disaggregates into small <5 mm clasts which are ejected in a near vertical direction. At ratios of 1.2 and 1.4, the disaggregation of the hemisphere is less apparent as fewer clasts are ejected.

At the greater depths of 5 and 10 cm, hemispheres that form are burst through by the heave event at the lowest ratios (0.45 to 0.75).

Beginning at the 0.9 ratio, hemispheres again begin to become burst controlled at the 10cm depth. This applies to the Pear and Slug (short) balloons; the Round balloon still produced a hemisphere which burst at this ratio - the maximum able to be tested.

At the 1.0 ratio and 5 cm depth, the Round and Slug (short) balloons now also produce hemispheres which are heaved through. This is not seen for the Pear balloon until the 1.2 ratio, where all of the 14 cm balloons at all depths produce the burst controlled hemispheres.

Within the Slug (long) balloon series all hemispheres are burst controlled at the 1.2 and 1.4 ratios. With the exception of the 0.5cm experiment at 0.5 ratio, all other hemispheres are heave controlled.

The implications of hemisphere collapse are discussed in Chapter 3.4.

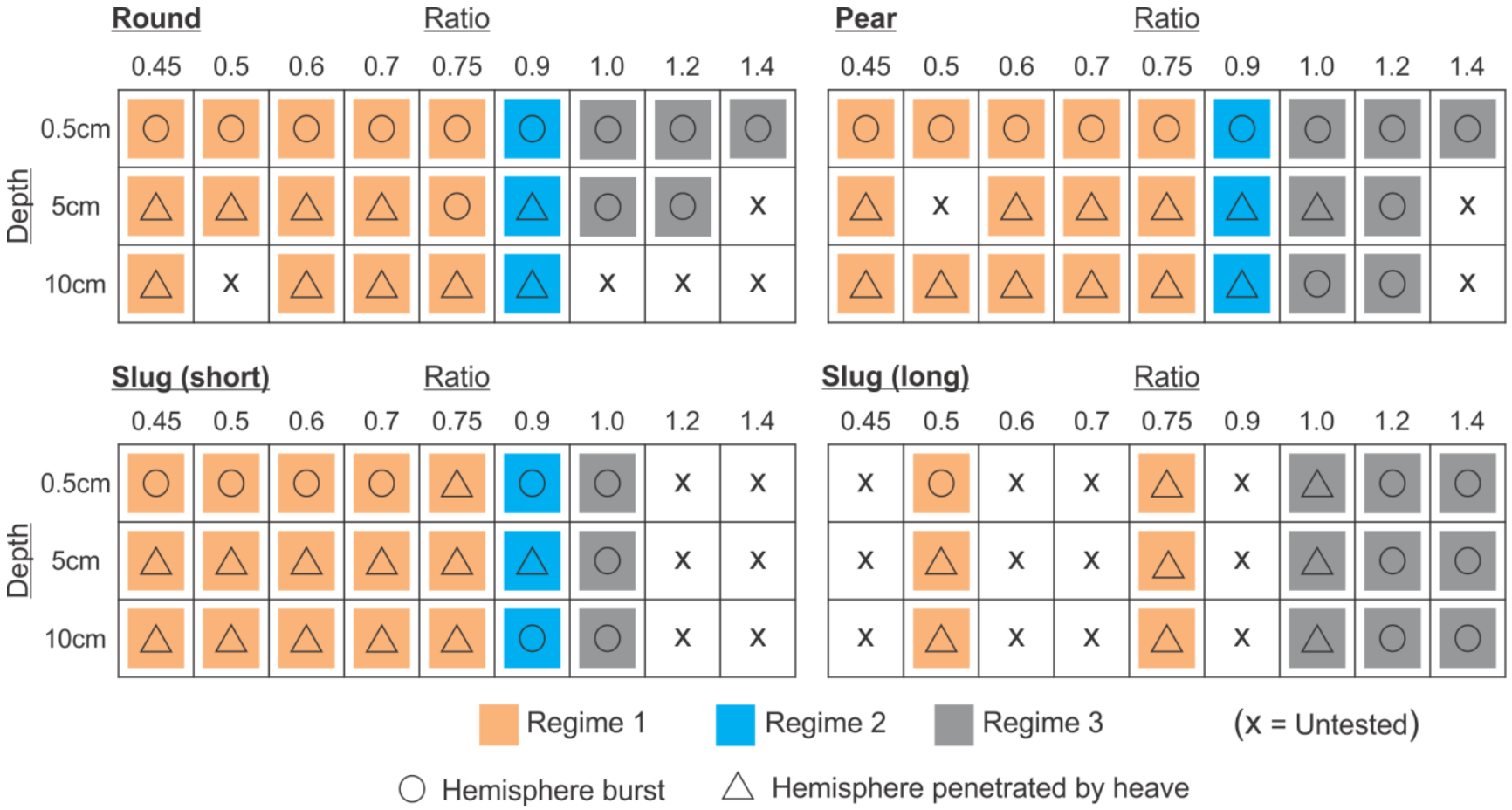

Figure 3.12: Overview of experiments by regime and hemisphere collapse.

3.3.2.5 **Experimental Regime Identification**

Experiments are subdivided into 3 regimes by behaviour, the boundaries of which are defined by kaolinite powder:water ratio. Each is based on the morphology of surface expressions. Descriptions are mostly combined for all four balloon types due to similarities between each rather than described separately. Regime figures display just the Pear balloon at 0.5 and 5 cm depth as these best illustrate each regime. Minor differences between types are discussed in Chapter 3.4. Regime boundaries are displayed in Figure 3.12.

Regime 1: Fluidal - Ratio 0.45 to 0.75

A regime characterised by spherical clasts and highly fluidal stringy mud features (Figure 3.13). At the shallowest balloon depth thin sheet-like heaves form from the Round and Pear balloons, and thinner but equally fluid-like heaves form from both the Slug balloons. Numerous spherical droplets are ejected by bursting of a primary but small hemisphere. Similar-shaped clasts form by separating from the heave. String-like structures from heave contraction and interaction with the burst hemisphere are common throughout. These strings further contract into spherical clasts upon breaking.

At the 5 and 10 cm depths heaves penetrate the primary hemispheres. At the 0.45 and 0.5 ratios heaves are difficult to distinguish but a common structure develops at ratios of 0.6 to 0.75. This structure consists of two sections - a wide basal section with a narrow upper section. Individual clasts are spherical but uncommonly ejected with the heaves. String structures are common with hemisphere penetration.

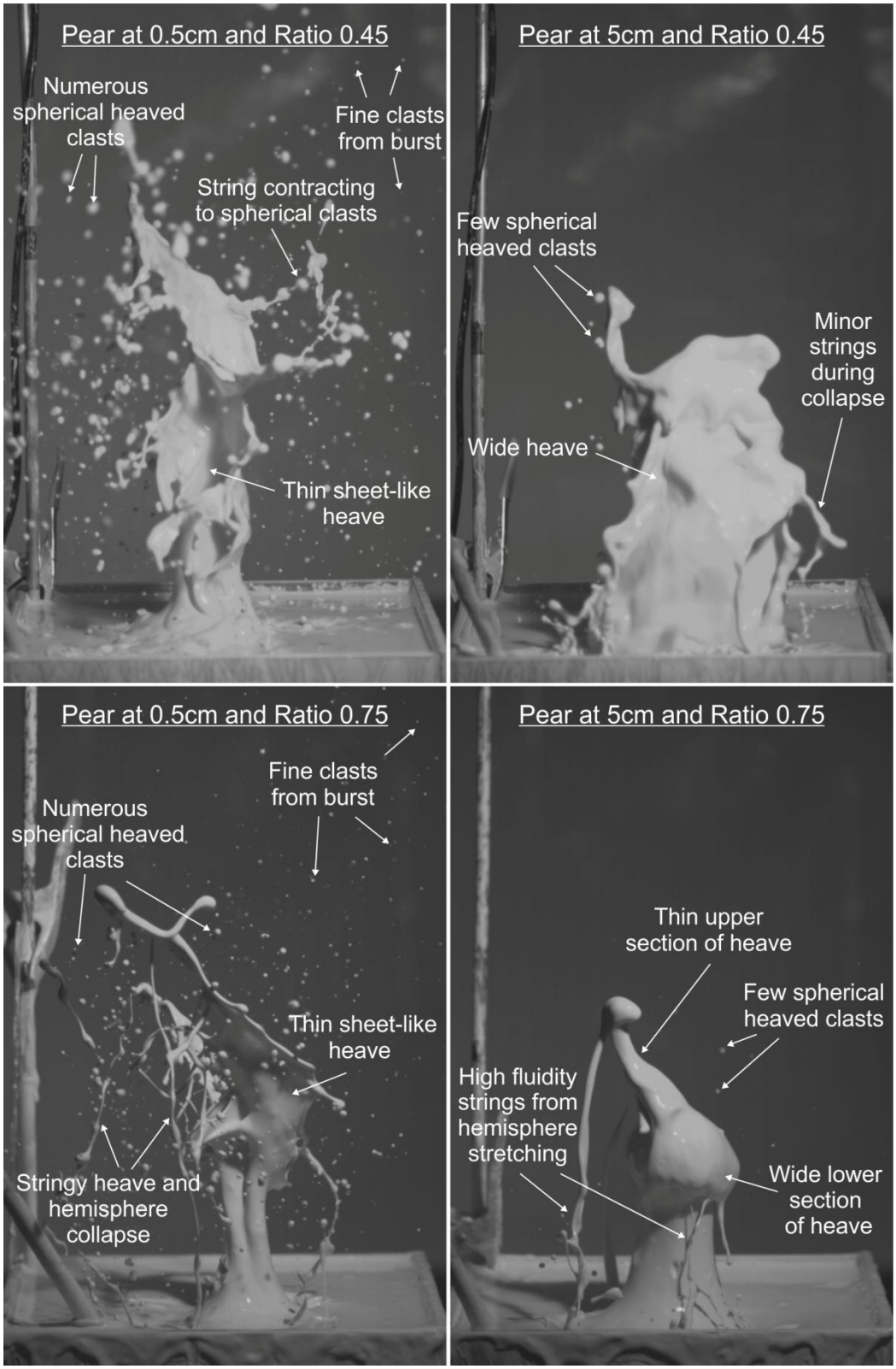

Figure 3.13: Experimental Regime 1 example. Images show range from 0.45 to 0.75 for Pear balloon at 0.5 and 5cm.

Regime 2: Transitional - Ratio 0.9

A less fluidal regime characterised by elongated clasts (Figure 3.14). At the shallowest depth bursting of the primary hemisphere ejects less spherical clasts than Regime 1. Heaves are narrow and form thin individual columns. String-like structures form from heave contraction and expansion of the burst hemisphere however clasts from string contraction are again less spherical than the previous regime.

At other depths heaves are similar to those of the 0.6 to 0.75 ratios of Regime 1 but are noticeably less fluidal in their collapse. Typically heaves again penetrate hemispheres instead of the bursting seen at shallow depths. Ejection of individual clasts is completely absent in all balloon experiments at these depths.

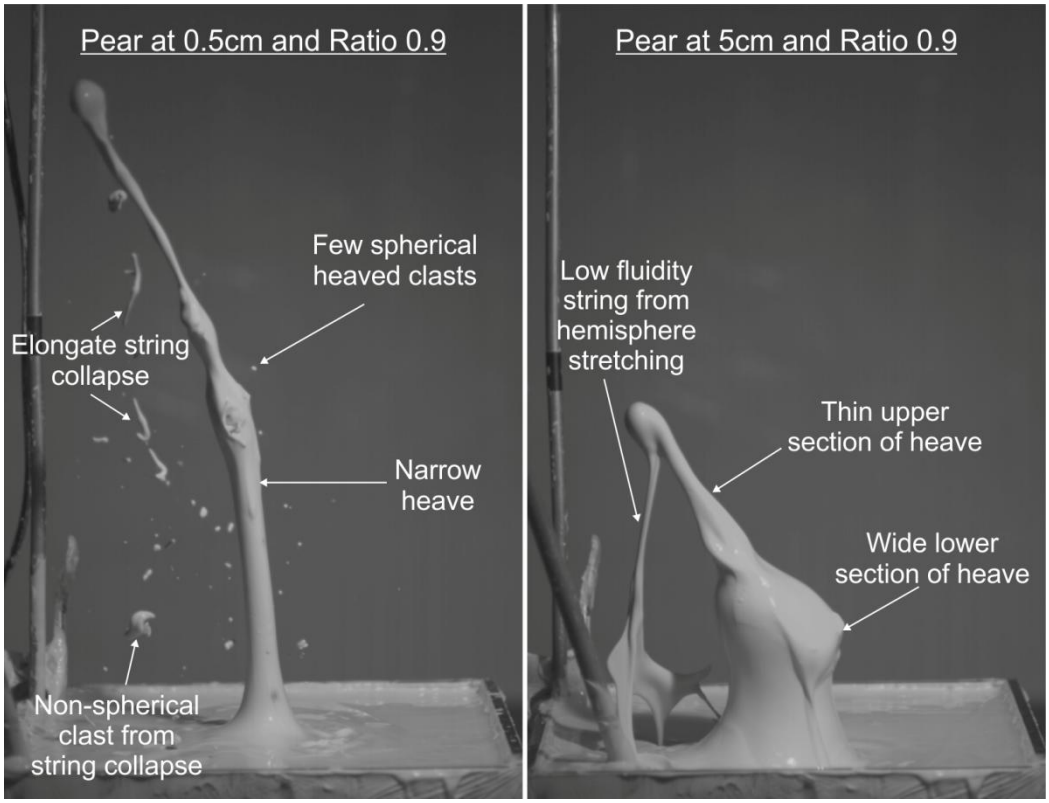

Figure 3.14: Experimental Regime 2 example. Images show 0.9 for Pear balloon at 0.5 and 5cm.

Regime 3: Brittle - Ratio 1.0 to 1.4

A regime characterised by the brittle bursting of hemispheres and where clasts maintain their shapes during hemisphere collapse and heave (Figure 3.15). Hemispheres grow well above the surface before bursting and fragmenting into angular flakes with no common size or shape. These flakes are ejected and maintain their shape until impact during ratios 1.2 and 1.4. Rounding of flake edges occurs at 1.0 but is still considered to be within this regime due to the brittle bursting nature. Where fragmentation of the hemisphere doesn't occur, i.e. where the lower edges remain connected to the mud surface, a petal-like effect is observed. This is created by an outward expansion of these attached thin flakes to form a shape similar to the petals of a flower. Heaves are still singular columns at the 1.0 ratio but are dominantly ejected as individual clasts at higher ratios when present.

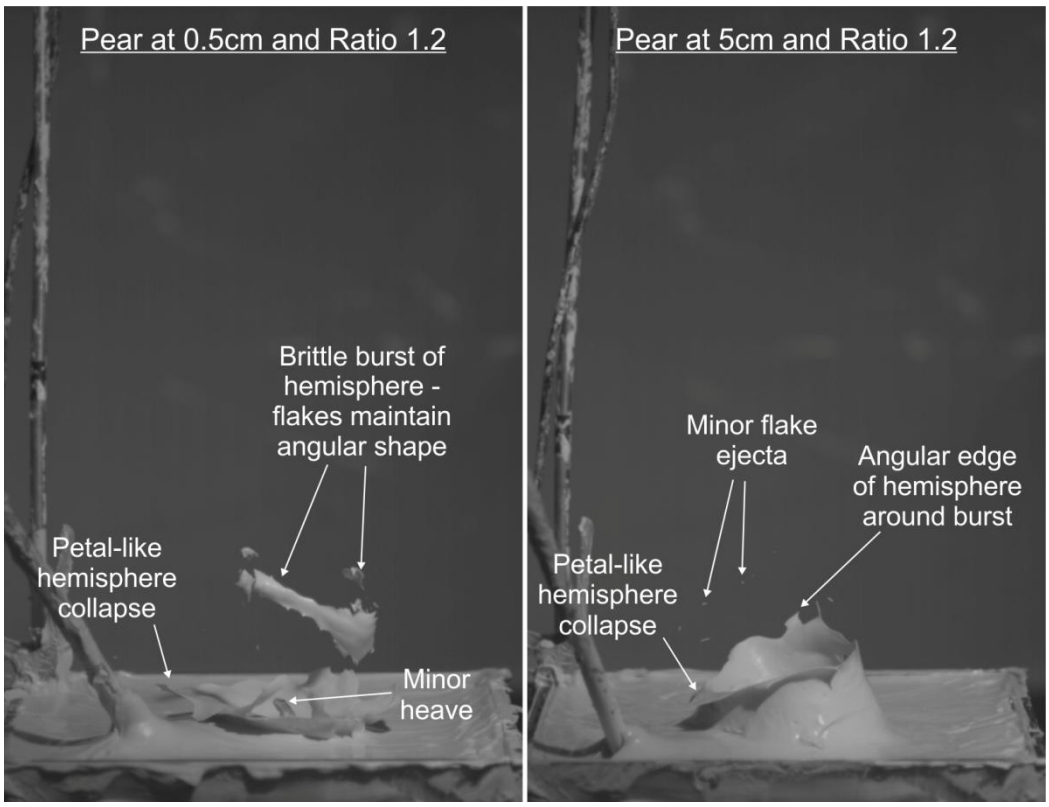

Figure 3.15: Experimental Regime 3 example. Images show 1.2 for Pear balloon at 0.5 and 5cm.

3.4 Discussion

3.4.1 Controls on surface expressions

Controls of bubble depth, viscosity and bubble length are discussed individually in this section. Interpretation of the influence of bubble shape on surface expression is less focused on but included where appropriate within each control discussion. This is due to the variations in bubble volume, width and pressure between balloon types and therefore the inability to directly compare them. However, two major difference are worth noting.

Heaves associated with Slug balloons are typically much narrower than the Pear and Round balloons. This corresponds with the initial narrow balloon shape and is possibly the result of a more channelised, narrow bubble rise and heave ejection. Also associated with the initial shape is hemisphere size, where the largest hemispheres occur with the largest initial balloon diameters.

Control 1: Bubble Depth

The depth of the initial balloon from the surface influences both the height of heaves produced and the diameters of hemispheres.

The highest heaves are consistently produced by balloons at the shallowest (0.5 cm) depth, while the lowest heaves correspond with balloons at the deepest depth (10cm). In only two cases of the main 83 experiments is this pattern not followed - in both the 5 cm depths at 1.2 ratio for the Pear and Slug (long) balloons. This difference is discussed in the next section on viscosity control.

A cause for these height variations can be determined by relating hemisphere burst or penetration with velocity data measured for the balloon bursts in water.

At 0.5 cm depth an initial slug (Figure 3.16-A) rises and very rapidly breaches the surface by bursting of a shallow hemisphere (Figure 3.16-B). Water bursts show this breach occurs while the bubble is still in the initial shortening phase. The tail is therefore ascending at the fastest rate observed during any stage of the ascent. The surface breach results in escape of the air/bubble volume and prevents the spherical bubble formation phase. Slowing of the tail associated with bubble shortening towards a sphere does still occur however it has no influence on the velocity of the heave as it has already erupted through the breach. The bursting of the hemisphere also means that a slowing of the heave by hemisphere interaction is non-existent (Figure 3.16-C) and a high heave is therefore produced (Figure 3.16-D).

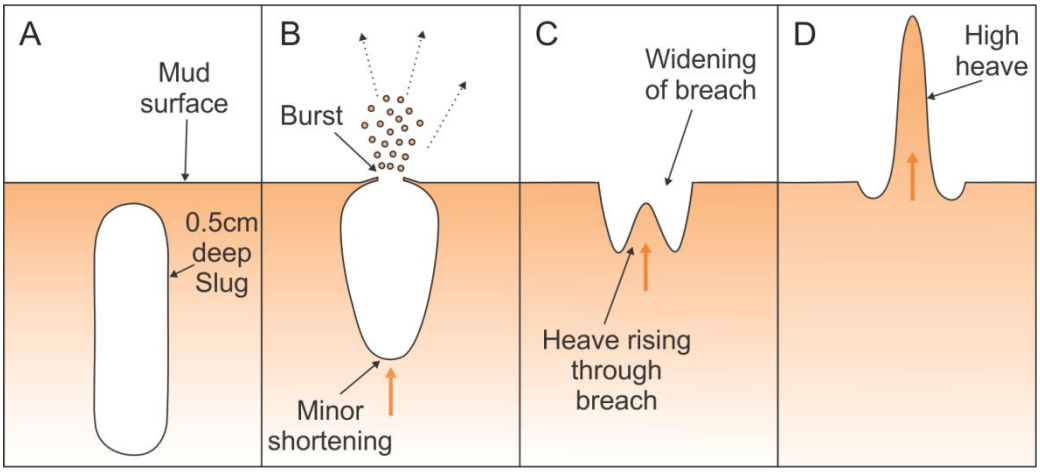

Figure 3.16: Bubble morphology evolution and formation of heave at 0.5cm bubble depth (cross-section). A - initial slug, B - rise of faster slug tail and rapid surface breaching of head, C - breach expansion and heave ascent, D - maximum heave. Brown arrows = motion of dragged mud by tail.

At 5 cm depth the full range of bubble morphology changes as in Figure 3.4 occurs. The ascent of bubble from an initial slug shape (Figure 3.17-A) results in shortening and lateral expansion of the upper bubble (Figure 3.17-B). Differing from burst and breach at 0.5 cm (Figure 3.16-B) no surface expression is yet seen. A hemisphere develops as the bubble further ascends and shortens (Figure 3.16-C). Continued ascent results in the growth of the hemisphere and inversion of the tail as the heave now penetrates the spherical bubble (Figure 3.16-D) Hemispheres become wider indicating maximum lateral expansion of the bubble. Slowing of the heave associated with shortening and penetration of the hemisphere results in a smaller heave than the 0.5 cm depth (Figure 3.16-E).

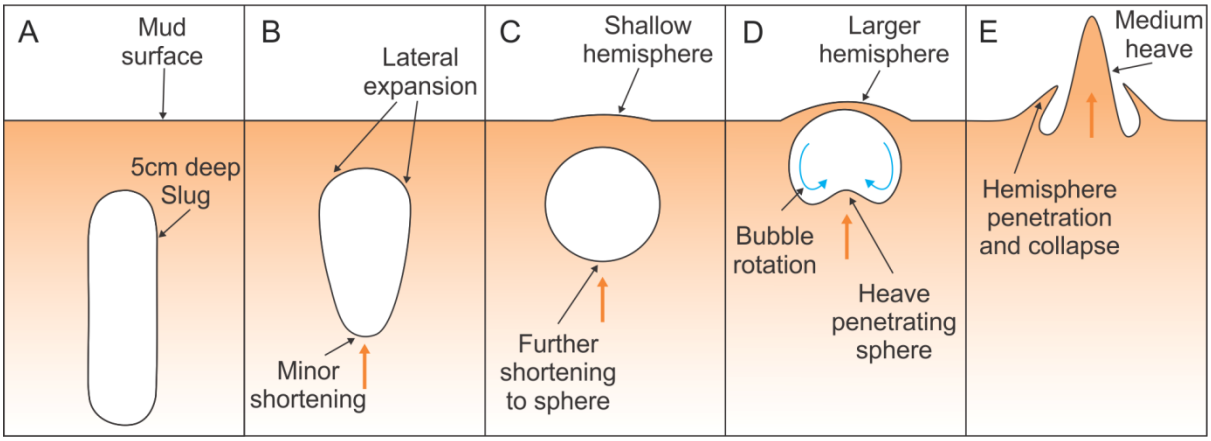

Figure 3.17: Bubble morphology evolution and formation of heave at 5cm bubble depth (cross-section). A - initial slug, B - rise of slug with faster ascent of tail, widening of top, C - further ascent and lateral expansion and shallow hemisphere, D - inversion of the tail, rotation of bubble and growth of hemisphere, E - heave penetration of hemisphere. Brown arrows = motion of dragged mud by tail.

At 10 cm depth the similar processes occur however depth has more influence on surface expression. An initial slug (Figure 3.18-A) ascends and shortens (Figure 3.18-B). With shortening to a sphere (Figure 3.18-C) and heave penetration of the still submersed bubble (Figure 3.18-D) there is still no visible hemisphere at the surface. This hemisphere only develops once the heave has intruded well into the bubble (Figure 3.18-E). Slowing of the heave associated with bubble shortening and penetration of a thicker hemisphere results in the lowest observed heaves (Figure 3.18-E).

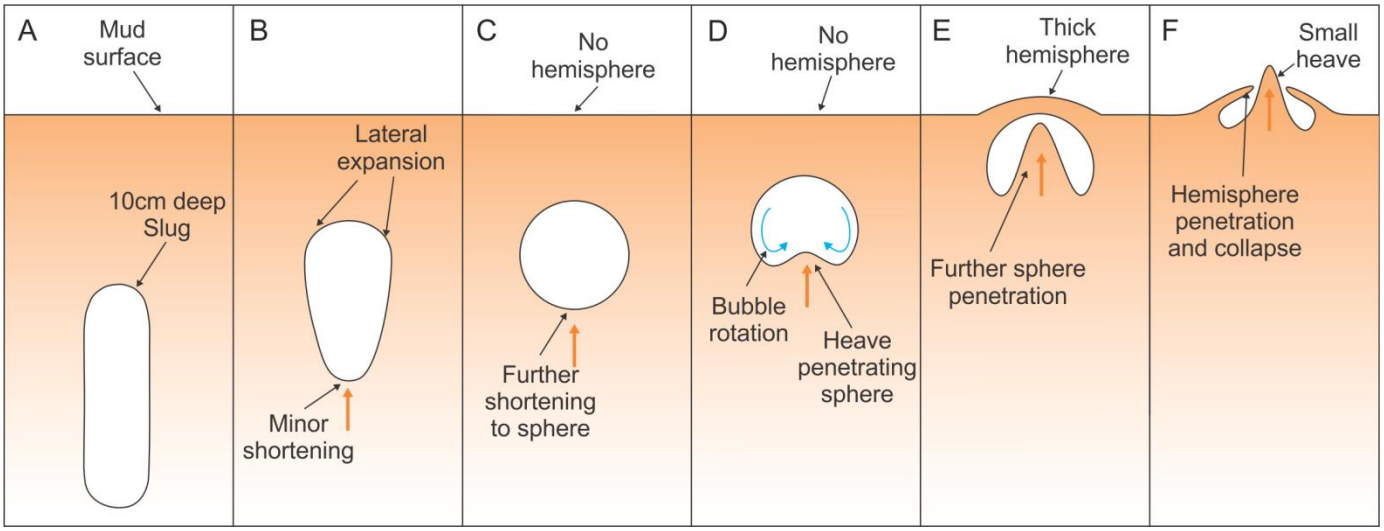

Figure 3.18: Bubble morphology evolution and formation of heave at 10cm bubble depth (cross-section). A - initial slug, B - rise of slug with faster ascent of tail, widening of top, C - shortening to sphere, D - inversion of tail, E - hemisphere formation and further heave ascent, F - heave penetration of hemisphere. Brown arrows = motion of dragged mud by tail.

.

Control 2: Viscosity

The viscosity, or ratio of kaolinite powder:water, influences heave heights and controls the observed regimes. No obvious influence on hemisphere diameter is observed until the 1.4 ratio.

There exists a generally consistent trend of decreasing heave heights as viscosity increases. Two exemptions to this are apparent though:

- Slug (short) balloons appear to have an initial increase in heave heights followed by the characteristic decrease seen in other balloon types.
- Heaves at the 10 cm depth and 1.2 ratio for Pear and Slug (long) balloons both eject higher than those at the same depth at 1.0 and 1.4 ratios. In both cases very thin strand or elongated strand sections are ejected.

It is unclear why heave heights in the above two points are different from other shapes, and other depths and ratios. Further investigation or repeated experiments would be required to determine the specific cause of these features.

Hemisphere diameters are relatively consistent per depth across viscosities until the 1.4 ratio where all balloons able to be tested show a decrease in width. This is particularly apparent in the Slug (long) balloon experiments where similar narrow hemisphere diameters are measured for each burst depth. These similar widths are an indication that lateral expansion associated with bubble shortening is strongly restricted and therefore the balloon may rise as a similar shape throughout.

Viscosity also has a control over whether a hemisphere collapses by bursting due to air pressure or collapses due to penetration by an ascending heave. This is turn indicates how fast the tail ascends per viscosity.

At 0.5 cm hemispheres burst almost instantly after they are observed on the surface until the 0.9 - 1.0 ratios (as per Figure 3.16-B). This burst is attributed to the inability of the narrow 0.5 cm film of mud

to contain the high pressure air volume of the bubble. As viscosity increases the mud film is less readily burst and grows to accommodate the rising bubble, producing very rounded hemispheres before bursting by internal air pressure. None of the hemispheres which form from the Pear, Round and Slug (short) balloons at this 0.5 cm depth are penetrated by heaves. Only the Slug (long) balloon related heaves at 0.75 and 1.0 ratios penetrate hemispheres at this depth.

At 5 and 10 cm depth the same rounded hemispheres begin forming at the 0.9 - 1.0 ratio. The hemispheres change from begin dominantly penetrated by heaves to dominantly burst controlled.

The transition from heave controlled to burst controlled hemisphere collapse in the 5 cm and 10 cm depth experiments indicates a change to the rate of ascent of the bubble tail. The heights of heaves formed by the dragging effect of the bubble tail are dependent on how quickly that tail is ascending. When heaves no longer burst through hemispheres, as a result of insufficient size or delayed expression, it infers that tail speeds relative to the bubble head have significantly decreased. In these cases mud is too viscous to drag as efficiently towards the surface as in fluidal regimes.

Finally, viscosity is the parameter that defines the regimes. At low viscosities heaves and hemispheres show fluidal behaviour, moving to brittle behaviour at higher viscosities.

Control 3: Bubble length

The length of the bubble has direct influence on the heave height but shows little influence on hemisphere diameters. For this section I discuss the experiments where shape was maintained but length was varied (i.e. the appropriate Slug balloon experiments).

A long bubble will produce a higher heave than that which forms with a shorter bubble. This is particularly apparent in the slug balloon experiments at the shallowest depths. Where Slug (long) and Slug (short) balloons were tested at the 0.5, 0.75 and 1.0 ratios, the heaves produced by the Slug (long) balloons were up to 2.1 m higher than the latter. This is a direct result of the fast moving tail of a longer slug bubble (Figure 3.5) ascending at higher velocities than the shorter slug bubble tails. Increased heights were also observed at the deeper depths of 5 and 10 cm however the difference was much less pronounced. In these cases the interaction with the hemisphere and/or slowing during shortening is a likely cause for this.

The length sequence of slug balloons at the 0.9 ratio confirms the effect of bubble length on heave height. In these experiments at 5 cm a consistent height increase of main heave columns corresponded with stepped 2 - 5 cm increases to slug length. The only exemption to absolute heave heights were when the top-most section of the heave columns fragmented a single clast which ascended higher.

Hemisphere width is consistent regardless of slug length. At the 0.5, 0.75 and 1.0 ratios the 14 and 24 cm Slug balloons produce hemispheres with similar diameters. The best comparison is within the 0.9 ratio series though, where hemisphere width only show a 1.5 cm variation between the smallest and largest hemispheres for all balloons between 14 and 25 cm lengths.

Chapter 4. Discussion

4.1 Implications for the evolution of the White Island eruptive episode

Some comparison can be made between observations from recordings of the January/February White Island eruptive episode and the mud experiments. As surface expressions were classified into regimes for each, the regimes are matched as accurately as possible (Table 4.1). Implications are made for the White Island activity from factors controlling the experimental regimes.

White Island Regime	Closest Experimental Regime	Likely Bubble Shape
1: Irregular bursting	1: Fluidal (close to Transitional)	Undefined at beginning, moving to more slug-like
2: Starbursting	3: Brittle	Slug
3: Burst, gas jet and heave	Similarities with shallow bursts and Regime 3	Long Slug
4: Dry mud venting	No similar regime	-

Table 4.1: White Island and Experimental Regime comparison table.

Counter to the mud experiments, a visual assessment of the mud pool showed that as mud viscosity increased so did heave heights during the White Island episode. Experiments show there are two ways to increase heights in this scenario; by either decreasing the bubble depth or increasing the bubble length. Minor changes to lake levels were observed during the episode with the difference between days being no more than ~1 meter. Therefore, the influence of depth is estimated to the lesser controlling factor to height. As such, I relate a systematic increase in bubble length during the first 3 White Island regimes as the controlling factor on heave height increase, counteracting any effect of viscosity.

Initial bubble shapes during the first days of Regime 1 may indeed be short and similar to the Round and Pear balloon shape. The low ~8 m heaves on the first two days appear similar to the 10 cm depth balloon experiments at low ratios, but with similar surface expressions for each of the 14 cm balloon types the actual White Island bubble shape is difficult to estimate.

The mud pool above the conduit allows a region for the lateral bubble expansion observed during bubble ascent in experiments. However, if bubble size increases occur at White Island, the conduit becomes the controlling factor on bubble shape. With lateral expansion restricted within the conduit, increases to bubble volumes would result in a lengthening and formation of a much more slug-like shape. Consistent hemisphere diameters at White Island support a bubble length increase as Slug balloon experiments formed similar-sized hemispheres regardless of length.

The starbursting of White Island Regime 2 is associated with the brittle bursting of Experimental Regime 3. The angular clasts of hemisphere disaggregation in producing the starburst effect indicate a brittle fragmentation mechanism. Although the starburst effect was not produced in experiments, possibly due to the smaller scale of experiments, hemispheres did display a brittle behaviour when ratios increased. These regimes correspond with a ratio of 1.0 and upwards where in order to produce a high heave a much longer balloon is required.

White Island Regime 3 of the burst, gas jet and heave was not explicitly observed in the mud experiments however similar features where observed in the shallow depth bursts. The white steam/gas jet was not visible in the experiments as compressed air was used for inflation. Fine clasts ejected near-vertically by the rapid bursting of hemispheres at the 0.5 cm depth are however a feature similar to the initial burst associated with the White Island gas jet. No hemisphere is seen to form during White Island Regime 3 though, not even a similar shallow hemisphere as in the experiments. Because of this the brittle fracturing mechanism above a long, high pressure slug as described in the discussion of Chapter 2 is favoured for this regime.

White Island Regime 4 was not reproduced in the experiments but I consider a near-constant gas/steam venting in the pool now devoid of all water as a likely mechanism in creating this regime. The rapid pulses rather than constant ejection imply some form of pressure build up and release, possibly a result of weak sealing between dry ash/lapilli and lithics within the conduit.

4.2 Future Research and ongoing work

Some data was not included in this thesis as the amount attained during experiments was greater than the scope of this project. This includes air streaming experiments at the same depths and ratios as the balloons, and acoustic analysis from infrasound recorded for all mud experiments. Scaling analysis of experiments is being prepared for comparison with the White Island observations and inclusion in the related paper.

Chapter 5. Conclusions

Research questions proposed at the beginning of this thesis and investigated by detailed analysis of the White Island episode and experimental bubble bursts, as presented in Chapters 2, 3 and 4, can be summarised into key points as follows:

- Phreatic bubble bursts at White Island became increasingly explosive as the mud pool desiccated. Heave heights increased from ~8 m to ~102 m as regimes moved from highly fluidal to brittle behaviour. The reverse occurred with a fluidal pool re-establishment.
- The most explosive activity (Regime 3) is identifiable in the seismo-acoustic record. This offers another mechanism for determining activity at White Island in the absence of visual monitoring.
- The evolution to more explosive behaviour has implications for lava lakes, geysers, and other volcanic and geothermal systems. Any changes to conditions at these may correspond to an increase in explosivity and introduce a ballistic hazard.

Experiments have shown that:

- Increasing the viscosity of mud, through decrease of the water fraction present, will reduce the height of heaves when bubble parameters are unchanged.
- Viscosity controls surface expressions in mud by transition from fluidal to brittle behaviour.
- Increasing the length of a slug bubble will increase the height of a heave, but has little influence on the size of the hemisphere which initially forms at the surface.
- Heave heights increase as bubble burst depth decreases.

Relating experiments to White Island show that:

- An increase in slug length was required to counter the effect of increasing mud pool viscosity on heave heights.
- A mud pool level drop may have also influenced the heave heights.
- The increased explosivity of hemisphere bursts from fluidal collapse to brittle 'starbursting' was a function of the mud viscoity.

Chapter 6. References

Abràmoff, M. D., Magalhães, P. J., & Ram, S. J. (2004). Image processing with ImageJ. *Biophotonics International*, *11*(7), 36-42.

Adelstein, E., Tran, A., Saez, C. M., Shteinberg, A., & Manga, M. (2014). Geyser preplay and eruption in a laboratory model with a bubble trap. *Journal of Volcanology and Geothermal Research*, *285*, 129-135.

Andrews, R. G., White, J. D., Dürig, T., & Zimanowski, B. (2014). Discrete blasts in granular material yield two-stage process of cavitation and granular fountaining. *Geophysical Research Letters*, *41*(2), 422-428.

Antipin, V. S., Pokrovsky, B. G., & Fedorov, A. M. (2015). Formation of the Patom Crater by phreatic explosion: Geological and isotope-geochemical evidence. *Lithology and Mineral Resources*, *50*(6), 478-487.

Barberi, F., Bertagnini, A., Landi, P., & Principe, C. (1992). A review on phreatic eruptions and their precursors. *Journal of Volcanology and Geothermal Research*, *52*(4), 231-246.

Black, P. M. (1970). Observations on White Island Volcano, New Zealand. *Bulletin Volcanologique*, *34*(1), 158-167.

Blackburn, E. A., Wilson, L., & Sparks, R. J. (1976). Mechanisms and dynamics of strombolian activity. *Journal of the Geological Society*, *132*(4), 429-440.

Bouche, E., Vergniolle, S., Staudacher, T., Nercessian, A., Delmont, J. C., Frogneux, M., Cartault, F., & Le Pichon, A. (2010). The role of large bubbles detected from acoustic measurements on the dynamics of Erta'Ale lava lake (Ethiopia). *Earth and Planetary Science Letters*, *295*(1), 37-48.

Brantley, S. L., Agustsdottir, A. M., & Rowe, G. L. (1993). Crater lakes reveal volcanic heat and volatile fluxes. In *GSA Today* (Vol. 3, No. 7, p. 4). Geological Society of America.

Browne, P. R. L., & Lawless, J. V. (2001). Characteristics of hydrothermal eruptions, with examples from New Zealand and elsewhere. *Earth-Science Reviews*, *52*(4), 299-331.

Bulletin of the Global Volcanism Network (BGVN) (1991) Caldera lake bubbling; burned vegetation, Vol. 16:07. Smithsonian Institute.

Burton, M., Allard, P., Muré, F., & La Spina, A. (2007). Magmatic gas composition reveals the source depth of slug-driven Strombolian explosive activity. *Science*, *317*(5835), 227-230.

Buttinelli, M., De Rita, D., Cremisini, C., & Cimarelli, C. (2011). Deep explosive focal depths during maar forming magmatic-hydrothermal eruption: Baccano Crater, Central Italy. *Bulletin of Volcanology*, *73*(7), 899-915.

Chardot, L., Jolly, A. D., Kennedy, B. M., Fournier, N., & Sherburn, S. (2015). Using volcanic tremor for eruption forecasting at White Island volcano (Whakaari), New Zealand. *Journal of Volcanology and Geothermal Research*, *302*, 11-23.

Chouet, B. A., Dawson, P. B., James, M. R., & Lane, S. J. (2010). Seismic source mechanism of degassing bursts at Kilauea Volcano, Hawaii: Results from waveform inversion in the 10–50 s band. *Journal of Geophysical Research: Solid Earth (1978–2012)*, *115*(B9).

Christenson, B. W., & Wood, C. P. (1993). Evolution of a vent-hosted hydrothermal system beneath Ruapehu Crater Lake, New Zealand. *Bulletin of Volcanology*, *55*(8), 547-565.

Cole, R. H. Underwater explosions, 1948. *Princeton UP*.

Cole, J. W., & Nairn, I. A. (1975). Catalogue of the active volcanoes and solfatara fields of New Zealand, Part XXII. In: Decker, R.W. (Ed.), Catalogue of the Active Volcanoes of the World

Including Solfatara Fields. International Association of Volcanology and Chemistry of the Earth's Interior, Rome, 38–49.

Cole J. W., Thordarson, T., & Burt, R. M. (2000), Magma Origin and Evolution of White Island (Whakaari) Volcano, Bay of Plenty, New Zealand. *J. Petrol*. *41*(6), 867-895.

Duncan, A.R. (1970). The petrology and petrochemistry of andesite volcanoes in Eastern Bay of Plenty, New Zealand. Ph.D. Thesis, Victoria University of Wellington, New Zealand.

Edmonds, M., & Gerlach, T. M. (2007). Vapor segregation and loss in basaltic melts. *Geology*, *35*(8), 751-754.

Fauria, K. E., & Rempel, A. W. (2011). Gas invasion into water-saturated, unconsolidated porous media: Implications for gas hydrate reservoirs. *Earth and Planetary Science Letters*, *312*(1), 188-193.

Fitzgerald, R. H., Tsunematsu, K., Kennedy, B. M., Breard, E. C. P., Lube, G., Wilson, T. M., Jolly, A. D., Pawson, J., Rosenberg, M. D., & Cronin, S. J. (2014). The application of a calibrated 3D ballistic trajectory model to ballistic hazard assessments at Upper Te Maari, Tongariro. *Journal of Volcanology and Geothermal Research*, *286*, 248-262.

Germanovich, L. N., & Lowell, R. P. (1995). The mechanism of phreatic eruptions. *Journal of Geophysical Research: Solid Earth (1978–2012)*, *100*(B5), 8417-8434.

Gerst, A., Hort, M., Aster, R. C., Johnson, J. B., & Kyle, P. R. (2013). The first second of volcanic eruptions from the Erebus volcano lava lake, Antarctica—Energies, pressures, seismology, and infrasound. *Journal of Geophysical Research: Solid Earth*, *118*(7), 3318-3340.

Giggenbach, W. F. (1974). The chemistry of Crater Lake, Mt Ruapehu (New Zealand) during and after the 1971 active period. *NZJ Sci*, *17*(1), 3346.

Giggenbach, W. F., & Glasby, G. P. (1977). The influence of thermal activity on the trace metal distribution in marine sediments around White Island, New Zealand. *DSIR Bulletin, 218*: 121-126.

GNS (2013). White Island Science Alert Bulletins. Institute of Geological and Nuclear Sciences, New Zealand Geological Survey, Lower Hutt.

Gurioli, L., Harris, A. J. L., Houghton, B. F., Polacci, M., & Ripepe, M. (2008). Textural and geophysical characterization of explosive basaltic activity at Villarrica volcano. *Journal of Geophysical Research: Solid Earth (1978–2012), 113*(B8).

Hedenquist, J. W., & Henley, R. W. (1985). Hydrothermal eruptions in the Waiotapu geothermal system, New Zealand; their origin, associated breccias, and relation to precious metal mineralization. *Economic geology*, *80*(6), 1640-1668.

Houghton, B. F., & Nairn, I. A. (1989). The phreatomagmatic and Strombolian eruption events at White Island volcano 1976-82: eruption narrative. *NZ Geol Surv Bull*, *103*, 13-23.

Houghton, B. F., & Nairn, I. A. (1991). The 1976–1982 Strombolian and phreatomagmatic eruptions of White Island, New Zealand: eruptive and depositional mechanisms at a 'wet'volcano. *Bulletin of Volcanology*, *54*(1), 25-49.

Hurst, A. W., Bibby, H. M., Scott, B. J., & McGuinness, M. J. (1991). The heat source of Ruapehu Crater Lake; deductions from the energy and mass balances. *Journal of Volcanology and Geothermal Research*, *46*(1), 1-20.

Hurst, A. W., Rickerby, P. C., Scott, B. J., & Hashimoto, T. (2004). Magnetic field changes on White Island, New Zealand, and the value of magnetic changes for eruption forecasting. *Journal of Volcanology and Geothermal Research*, *136*(1), 53-70.

Ichihara, M., Ripepe, M., Goto, A., Oshima, H., Aoyama, H., Iguchi, M., Tanaka, K., & Taniguchi, H. (2009). Airwaves generated by an underwater explosion: Implications for volcanic infrasound. *Journal of Geophysical Research: Solid Earth (1978–2012)*, *114*(B3).

Ilanko, T., Oppenheimer, C., Burgisser, A., & Kyle, P. (2015). Transient degassing events at the lava lake of Erebus volcano, Antarctica: Chemistry and mechanisms. *GeoResJ*, *7*, 43-58.

James, M. R., Lane, S. J., Chouet, B., & Gilbert, J. S. (2004). Pressure changes associated with the ascent and bursting of gas slugs in liquid-filled vertical and inclined conduits. *Journal of Volcanology and geothermal Research*, *129*(1), 61-82.

Jaupart, C., & Vergniolle, S. (1988). Laboratory models of Hawaiian and Strombolian eruptions. *Nature*, *331*(6151), 58-60.

Jaupart, C., & Vergniolle, S. (1989). The generation and collapse of a foam layer at the roof of a basaltic magma chamber. *Journal of Fluid Mechanics*, *203*, 347-380.

Jolly, A. D., Chardot, L., Neuberg, J., Fournier, N., Scott, B. J., & Sherburn, S. (2012). High impact mass drops from helicopter: A new active seismic source method applied in an active volcanic setting. *Geophysical Research Letters*, *39*(12).

Jolly, A. D., Kennedy, B. M., Edwards, M., Jousset, P., & Scheu, B. (in review). Infrasound tremor from bubble burst eruptions in the viscous shallow crater lake of White Island, New Zealand, and its implications for interpreting volcanic source processes.

Johnson, J., Aster, R., Jones, K. R., Kyle, P., & McIntosh, B. (2008). Acoustic source characterization of impulsive Strombolian eruptions from the Mount Erebus lava lake. *Journal of Volcanology and Geothermal Research*, *177*(3), 673-686.

Kato, A., Terakawa, T., Yamanaka, Y., Maeda, Y., Horikawa, S., Matsuhiro, K., & Okuda, T. (2015). Preparatory and precursory processes leading up to the 2014 phreatic eruption of Mount Ontake, Japan. *Earth, Planets and Space*, *67*(1), 1-11.

Kusakabe, M. (1996). *Hazardous crater lakes* (pp. 573-598). Springer Berlin Heidelberg.

Letham-Brake, M. (2013). Geological constraints on fluid flow at Whakaari volcano (White Island). M.Sc. Thesis. Department of Geological Sciences, University of Canterbury, Christchurch, New Zealand.

Lyons, J. J., Waite, G. P., Rose, W. I., & Chigna, G. (2010). Patterns in open vent, strombolian behavior at Fuego volcano, Guatemala, 2005–2007. *Bulletin of Volcanology*, *72*(1), 1-15.

Mastin, L. G. (1991). The roles of magma and groundwater in the phreatic eurptions at Inyo Craters, Long Valley Caldera, California. *Bulletin of Volcanology*, *53*(8), 579-596.

Mastin, L. G. (2001), A simple calculator of ballistic trajectories for blocks ejected during volcanic eruptions: U.S. Geological Survey Open-File Report 01-45, 16p, http://pubs.usgs.gov/of/2001/0045/

Mayer, K., Scheu, B., Gilg, H. A., Heap, M. J., Kennedy, B. M., Lavallée, Y., Letham-Brake, M., & Dingwell, D. B. (2015). Experimental constraints on phreatic eruption processes at Whakaari (White Island volcano). *Journal of Volcanology and Geothermal Research*, *302*, 150-162.

Mongillo, M. A., & Wood, C. P. (1995). Thermal infrared mapping of White Island volcano, New Zealand. *Journal of Volcanology and Geothermal Research*, *69*(1), 59-71.

Moon, V., Bradshaw, J., Smith, R., de Lange, W. (2005). Geotechnical characterization of stratocone crater wall sequences, White Island volcano, New Zealand. *Eng. Geol. 81*(2), 146–178.

Moon, V., Bradshaw, J., & de Lange, W. (2009). Geomorphic development of White Island Volcano based on slope stability modelling. *Engineering Geology*, *104*(1), 16-30.

Morrissey, M., Gisler, G., Weaver, R., & Gittings, M. (2010). Numerical model of crater lake eruptions. *Bulletin of Volcanology*, *72*(10), 1169-1178.

Namiki, A., Muñoz-Saez, C., & Manga, M. (2014). El Cobreloa: A geyser with two distinct eruption styles. *Journal of Geophysical Research: Solid Earth*, *119*(8), 6229-6248.

Nishi, Y., Sherburn, S., Scott, B. J., & Sugihara, M. (1996). High-frequency earthquakes at White Island volcano, New Zealand: insights into the shallow structure of a volcano-hydrothermal system. *Journal of Volcanology and Geothermal Research*, *72*(3), 183-197.

Ohba, T., Taniguchi, H., Miyamoto, T., Hayashi, S., & Hasenaka, T. (2007). Mud plumbing system of an isolated phreatic eruption at Akita Yakeyama volcano, northern Honshu, Japan. *Journal of Volcanology and Geothermal Research*, *161*(1), 35-46.

Okada, H.. (Pers. comms.). University of Hokkaido, Japan.

Pioli, L., Bonadonna, C., Azzopardi, B. J., Phillips, J. C., & Ripepe, M. (2012). Experimental constraints on the outgassing dynamics of basaltic magmas. *Journal of Geophysical Research: Solid Earth (1978–2012)*, *117*(B3).

Ross, P. S., & White, J. D. L. (2006). Debris jets in continental phreatomagmatic volcanoes: A field study of their subterranean deposits in the Coombs Hills vent complex, Antarctica. *J. Volcanol. Geotherm. Res.*, *149*, 62–84.

Ross, P.-S., White, J. D. L., Zimanowski, B., & Büttner, R. (2008). Multiphase flow above explosion sites in debris-filled volcanic vents: Insights from analogue experiments, *J. Volcanol. Geotherm. Res.*, *178*, 104–112.

Sánchez, C., Álvarez, B., Melo, F., & Vidal, V. (2014). Experimental modeling of infrasound emission from slug bursting on volcanoes. *Geophysical Research Letters*, *41*(19), 6705-6711.

Saptadji, N. M. (1995). Modeling of geysers. Ph.D. Thesis. Department of Engineering Science, University of Auckland, Auckland, New Zealand.

Sawyer, G. M., Carn, S. A., Tsanev, V. I., Oppenheimer, C., & Burton, M. (2008). Investigation into magma degassing at Nyiragongo volcano, Democratic Republic of the Congo. *Geochemistry, Geophysics, Geosystems*, *9*(2).

Sillitoe, R. H. (1994). Erosion and collapse of volcanoes: Causes of telescoping in intrusion-centered ore deposits. *Geology*, *22*(10), 945-948.

Taddeucci, J., Alatorre-Ibarguengoitia, M. A., Palladino, D. M., Scarlato, P., & Camaldo, C. (2015). High-speed imaging of Strombolian eruptions: Gas-pyroclast dynamics in initial volcanic jets. *Geophysical Research Letters*, *42*(15), 6253-6260.

Thevenaz, P., Ruttimann, U. E., & Unser, M. (1998). A pyramid approach to subpixel registration based on intensity. *Image Processing, IEEE Transactions on*, *7*(1), 27-41.

Tran, A., Rudolph, M. L., & Manga, M. (2015). Bubble mobility in mud and magmatic volcanoes. *Journal of Volcanology and Geothermal Research*, *294*, 11-24.

Trunk, L., & Bernard, A. (2008). Investigating crater lake warming using ASTER thermal imagery: Case studies at Ruapehu, Poás, Kawah Ijen, and Copahué Volcanoes. *Journal of Volcanology and Geothermal Research*, *178*(2), 259-270.

Ulivieri, G., Ripepe, M., & Marchetti, E. (2013). Infrasound reveals transition to oscillatory discharge regime during lava fountaining: Implication for early warning. *Geophysical Research Letters*, *40*(12), 3008-3013.

Valentine, G. A., Graettinger, A. H., & Sonder, I. (2014). Explosion depths for phreatomagmatic eruptions. *Geophysical Research Letters*, *41*(9), 3045-3051.

Vergniolle, S., & Brandeis, G. (1996). Strombolian explosions: 1. A large bubble breaking at the surface of a lava column as a source of sound. *Journal of Geophysical Research: Solid Earth (1978–2012)*, *101*(B9), 20433-20447.

Watson, Z. T., Han, W. S., Keating, E. H., Jung, N. H., & Lu, M. (2014). Eruption dynamics of CO 2-driven cold-water geysers: Crystal, Tenmile geysers in Utah and Chimayó geyser in New Mexico. *Earth and Planetary Science Letters*, *408*, 272-284.

Werner, C., Hurst, T., Scott, B., Sherburn, S., Christenson, B. W., Britten, K., Cole-Baker, J., & Mullan, B. (2008). Variability of passive gas emissions, seismicity, and deformation during crater lake growth at White Island Volcano, New Zealand, 2002–2006. *Journal of Geophysical Research: Solid Earth (1978–2012)*, *113*(B1).

Wright, I. C. (1992). Shallow structure and active tectonism of an offshore continental back-arc spreading system: the Taupo Volcanic Zone, New Zealand. *Marine Geology*, *103*(1), 287-309.